

TROPOSPHERIC EMISSION SPECTROMETER (TES)

LEVEL 2 ALGORITHM THEORETICAL BASIS DOCUMENT APPENDIX

Reinhard Beer	Jet Propulsion Laboratory
Kevin W. Bowman	Jet Propulsion Laboratory
Patrick D. Brown	Atmospheric and Environmental Research Inc.
Shepard A. Clough	Atmospheric and Environmental Research Inc.
Annmarie Eldering	Jet Propulsion Laboratory
Aaron Goldman	University of Denver
Michael Lampel	Raytheon
Mingzhao Luo	Jet Propulsion Laboratory
Frank J. Murcray	University of Denver
Gregory B. Osterman	Jet Propulsion Laboratory
Curtis P. Rinsland	NASA Langley Research Center
Clive D. Rodgers	University of Oxford
Mark Shephard	Atmospheric and Environmental Research Inc.
Susan E. Sund	Jet Propulsion Laboratory
Helen M. Worden	Jet Propulsion Laboratory
John Worden	Jet Propulsion Laboratory

Approved by:
Reinhard Beer
TES Principal Investigator

Version 1.16
June 27, 2002

Jet Propulsion Laboratory
California Institute of Technology
Pasadena, California

This document was prepared at the Jet Propulsion Laboratory, California Institute of Technology, under a contract from the National Aeronautics and Space Administration

TABLE OF CONTENTS

TABLE OF CONTENTS	I
LIST OF FIGURES	IV
LIST OF TABLES	IV
APPENDICES	1
A3.3.1: RADIATIVE TRANSFER	1
A3.3.1.1: Ray Tracing and Path Integrals	3
A3.3.1.1.1 Hydrostatic Equation	3
A3.3.1.1.2 Ray tracing in the nadir case.	4
A3.3.1.1.3 Path integrals in the nadir case	4
A3.3.1.1.4 Ray Tracing in the Limb Case	5
A3.3.1.1.5 Path Integrals for the Limb Case	8
A3.3.1.1.6 Ray tracing in the Inhomogeneous Limb Case.	8
A3.3.1.1.7 The gas equation for air	10
A3.3.1.1.8 Refractive index of air	11
A3.3.1.5: NON-LTE	12
A3.3.1.5.1:Non-LTE:NO Example	14
A3.3.2.2: MAP OF EARTH SURFACE COMPOSITION	19
A3.3.3 RADIATIVE TRANSFER FOR CLOUDS AND AEROSOLS	20
A3.3.3 Radiative Transfer for Clouds and Aerosols	20
A3.3.8.1: Line-by-Line Spectral Parameters	21
A3.3.8.2: Cross-Section P-T Interpolation Program XSFINT	27
A3.4: ANALYTIC JACOBIANS	31
A3.4.1 PARTIALS WITH RESPECT TO LAYER OPTICAL DEPTH (OD)	
$\frac{\partial L_{sat}}{\partial \tau_l}$	33

A3.4.1.1 Downwelling OD partials	$\frac{\partial L_0^\downarrow}{\partial \tau_l}$	33
A3.4.1.2 Upwelling OD partials	$\frac{\partial L_L^\uparrow}{\partial \tau_l}$	34
A3.4.2 PARTIALS OF OPTICAL DEPTH WITH RESPECT TO GAS SPECIES VMR	$\frac{\partial \tau_l}{\partial x_l}$	35
A3.4.2.1 Partial of optical depth with respect to H₂O VMR	$\frac{\partial \tau_l}{\partial q_{l,m=1}}$	36
A3.4.2.1.1 H ₂ O line self-broadening dependence	$\tau_{l,1}^{line} \frac{\partial \ln \kappa_{l,1}^{line}}{\partial \ln q_{l,1}}$	36
A3.4.2.1.2 H ₂ O continuum dependence	$\tau_{l,1}^{cont} \frac{\partial \ln \kappa_{l,1}^{cont}}{\partial \ln q_{l,1}}$	37
A3.4.2.1.3 Layer integrated path amount dependence on H ₂ O VMR	$\tau_l \frac{\partial \ln u_l}{\partial \ln q_{l,1}}$	37
A3.4.3 PARTIALS WITH RESPECT TO LAYER PLANCK (OR EFFECTIVE PLANCK) FUNCTION	$\frac{\partial L_{sat}}{\partial B_l}$	38
A3.4.4 PARTIALS OF LAYER PLANCK (OR EFFECTIVE PLANCK) FUNCTION WITH RESPECT TO TEMPERATURE	$\frac{\partial B_l}{\partial T_l}$	38
A3.4.5 PARTIALS OF OPTICAL DEPTH WITH RESPECT TO TEMPERATURE	$\frac{\partial \tau_l}{\partial T_l}$	39
A3.4.5.1 Partial of line absorption with respect to temperature	$\frac{\partial \kappa_{l,m}^{line}}{\partial T_l}$	39
A3.4.5.2 Partial of continuum absorption with respect to temperature	$\frac{\partial \kappa_{l,m}^{cont}}{\partial T_l}$	40

A3.4.5.2.1 Temperature partials for water vapor continuum coefficient $\frac{\partial C_{H_2O}}{\partial T_l}$	40
A3.4.5.2.2 Temperature partials for carbon dioxide continuum coefficient $\frac{\partial C_{CO_2}}{\partial T_l}$	41
A3.4.5.2.3 Temperature partials for nitrogen continuum coefficient $\frac{\partial C_{N_2}}{\partial T_l}$	41
A3.4.5.2.4 Temperature partials for oxygen continuum coefficient $\frac{\partial C_{O_2}}{\partial T_l}$	41
A3.4.5.3 Partial of layer integrated path amounts with respect to temperature $\frac{\partial u_{l,m}}{\partial T_l}$	41
A3.4.6 LAYER-TO-LEVEL JACOBIANS	42
A3.4.6.1 Limb layer-to-level VMR Jacobians	42
A3.4.6.2 Limb layer-to-level Temperature Jacobians	43
A3.4.6.3 Nadir layer-to-level VMR Jacobians	44
A3.4.6.4 Nadir layer-to-level Temperature Jacobians	44
A3.4.7 POINTING JACOBIANS	44
A3.4.8 JACOBIAN VALIDATION	46
A3.4.8.1 Nadir Jacobian Validation	46
A3.4.8.2 Limb Jacobian Validation	48
A3.5.1 RETRIEVAL STRATEGY	ERROR! BOOKMARK NOT DEFINED.
REFERENCES	53

LIST OF FIGURES

Figure A-1: Earth Geometric Model	1
Figure A-2: Propagation of a refracted ray through the limb	6
Figure A-3: NO kinetic, $v=1$, and $v=2$ vibrational temperatures in the daytime. Digitized from Funke and Puertas [2000].	14
Figure A-4: NO kinetic, $v=1$, and $v=2$ vibrational temperatures in the nighttime. Digitized from Funke and Puertas [2000].	15
Figure A-5: US standard atmosphere profiles of NO mixing ratio and temperature [Anderson et. al., 1986].	16
Figure A-6: TES LBLRTM computed spectra of NO under Non-LTE ($v=1$) daytime conditions for a limb path with a tangent height of 15 km. The results are plotted in both brightness temperature (top) and radiance (bottom).	17
Figure A-7: Difference plot between TES LBLRTM calculated radiances under Non-LTE ($v=1$) and LTE (kinetic temperature) conditions.	18
Figure A-8: Layer and level view for downwelling OD jacobian calculation	34
Figure A-9: Layer and level view for upwelling OD jacobian calculation	35
Figure A-10:	46
Figure A-11:	48
Figure A-12:	49

LIST OF TABLES

Table A-1: Summary of results for Non-LTE vs. LTE TES LBLRTM calculations.	19
Table A-2: USGS Land Use/Land Cover System Legend and Assignment of Material Type from the ASTER Spectral Library (http://speclib.jpl.nasa.gov/)	20
Table A-3: Nadir jacobian comparisons: Finite Difference (FD) to Analytic	46
Table A- 4: Limb jacobian comparisons: Finite Difference (FD) to Analytic	48

THIS PAGE INTENTIONALLY LEFT BLANK

APPENDICES

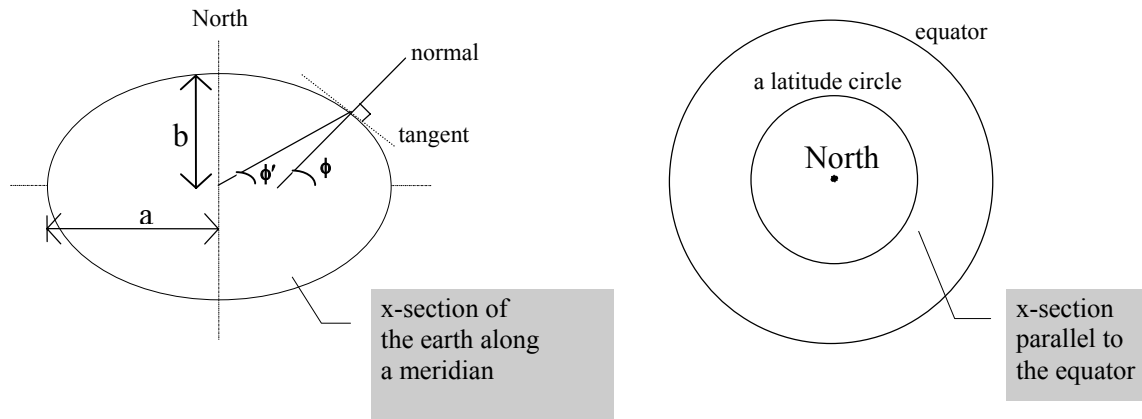
A3.3.1: Radiative Transfer

The Radius of Curvature of the Earth's Surface for a Given TES Limb Tangent Latitude and Viewing Direction

The ray-tracing step in Level 2 process uses Snell's Law for a spherically symmetric atmosphere to determine the bending along the ray. The radius of the "sphere" is considered to be the sum of the altitude and the *radius of curvature of the Earth surface* (not the Earth-centered radius) at the given location in the given direction. This Appendix presents the equations for the radius of the Earth surface curvature at a given latitude (TES limb tangent latitude) for TES viewing direction.

A very commonly used Earth geometric model is an ellipsoidal shape as illustrated below.

Figure A-1: Earth Geometric Model



Definitions of some parameters:

- a — equatorial radius (the semi-major axis of the meridian ellipse).
- b — polar radius (the semi-minor axis of the meridian ellipse).
- f — flattening factor.
- e — Earth ellipsoid eccentricity.
- ϕ — geodetic latitude as illustrated above.
- ϕ' — geocentric latitude as illustrated above.

Their relationships:

$$\tan(\phi) = \frac{\tan(\phi')}{(1-f)^2}; \quad (\text{A.1})$$

$$f = \frac{a-b}{a} ; \text{ and} \quad (\text{A.2})$$

$$e = \sqrt{2f - f^2} . \quad (\text{A.3})$$

There are two principle curvatures on the model Earth surface at a given location, the meridian curvature (North-South curvature) and the East-West curvature. The tangents of these two curvature are perpendicular. The East-West curvature plane is defined by the tangent along a latitude circle and the local normal. The equations for the radius of these two principle curvature planes are:

Radius of curvature in the North-South plane:

$$R_{NS} = \frac{a(1-e^2)}{(1-e^2 \sin^2 \phi)^{3/2}} . \quad (\text{A.4})$$

Radius of curvature in the East-West plane:

$$R_{EW} = \frac{a}{(1-e^2 \sin^2 \phi)^{1/2}} . \quad (\text{A.5})$$

TES always looks straight backward along the orbit. The orbit has 98.21° inclination angle which is the angle between the equatorial plane and the orbital plane. The parameter to define the TES viewing direction at its limb tangent point or any point along its line of sight is the azimuth angle (A_Z). The azimuth angle is the angle between the local meridian plane (the N-S plane) and the plane defined by the local normal and the tangent along the TES viewing direction. Under the spherical approximation, A_Z can be calculated as

$$\sin(A_Z) = \frac{\cos(\text{inclination_angle})}{\cos(\text{geocentric_latitude}, \phi')} . \quad (\text{A.6})$$

The EOS Toolkit provides a program to calculate a more rigorous azimuth without the spherical approximation (PGS_CSC_ZenithAzimuth). The viewing vector however, in the ECR (Earth Centered Rotating) coordinate system, needs to be defined.

The radius of the curvature in azimuth A_Z (R_C) can be calculated as

Radius of curvature in azimuth A_Z :

$$\frac{1}{R_C} = \frac{\cos^2(A_Z)}{R_{NS}} + \frac{\sin^2(A_Z)}{R_{EW}} . \quad (\text{A.7})$$

A3.3.1.1: Ray Tracing and Path Integrals

For ray tracing and path integrals, we require the following elements from the retrieval vector, at a set of levels $j=0..n$ in $\ln(P)$, and in the limb case when the atmosphere is not horizontally homogeneous, also at a set of locations along the line of sight:

T_j	level temperatures
q_{jm}	level mixing ratios for molecule m
P_s	surface pressure
T_s	surface temperature

and the following forward model parameters:

z_s	altitude of the surface relative to the geoid
R_c	radius of the geoid at the measurement location
R_{cs}	altitude of the spacecraft from the center of curvature of the geoid
θ_s	angle of ray at the satellite

The level quantities in the retrieval vector are interpolated at a finer spacing to give the full grid level values q_k^m and T_k .

A3.3.1.1.1 Hydrostatic Equation

The total air density ρ_k is computed from the gas equation at each full grid level. This must allow for the water content of the air, but the other minor constituents may be ignored [except possibly CO₂] (see Appendix 3.3.1.1.7). The hydrostatic equation may be written

$$dz = -[P/\rho(P)g(z)] d \ln(P) \quad (\text{A.8})$$

As the quantity $[P/\rho(z)g(z)]$ is close to RT/Mg , from the ideal gas equation, we take it to be linear in $\ln(P)$ over each layer. Hence the layer thickness is

$$z_k - z_{k-1} = (P_{k-1}/r_{k-1}g_{k-1} + P_k/\rho_k g_k)[\ln(P_{k-1}) - \ln(P_k)]/2 \quad (\text{A.9})$$

from the trapezoidal rule. The acceleration due to gravity is given as a function of height and latitude, and it consists of gravitational and rotational parts,

$$g(\phi, z) = g_{\text{grav}}(\phi, 0)[(R_e)/(R_e + z)]^2 - \Omega^2 N[(N+z)/R_e \cos \phi]^2 \quad (\text{A.10})$$

where Ω is the Earth's rotational angular frequency; $N = a^2 \sqrt{(a^2 - (a^2 - b^2) \sin^2 \phi)}$; and a and b is the semi-major and minor axis of earth respectively. The gravitational term at the earth surface is given by [International Gravity Formula, 1980]

$$g(\phi, 0) = 978.0327(1.0 + 0.0052790414 \sin^2 \phi + 0.0000232718 \sin^4 \phi + 0.0000001262 \sin^6 \phi) \quad (\text{A.11})$$

and,

$$g_{\text{grav}}(\phi, 0) = g(\phi, 0) - g_{\text{rot}}(\phi, 0). \quad (\text{A.12})$$

Note that equation (A.12) requires $g_k = g(z_k)$ before z_k has been computed. The effect is small and can be accommodated by several different ways, of which the simplest might be to approximate g_k by its value at an altitude given by $2z_{k-1} - z_{k-2}$.

A3.3.1.1.2 Ray tracing in the nadir case.

The zenith angle of the ray at each level is given by Snell's law in spherical symmetry:

$$\sin \theta_k = [R_{cs} \sin \theta_s] / [(R_c + z_k) n_k] \quad (\text{A.13})$$

where the refractive index n_k is given in section A3.3.1.1.8. However as $n_k \sim 1.0002$ at the surface, it may be ignored, incurring an error of only 0.02% in $\sin \theta_k$, and hence a similarly small amount in path length through $\sec \theta_k$.

A3.3.1.1.3 Path integrals in the nadir case

We need to evaluate the number of molecules per unit area in each layer, together with appropriately weighted mean pressures and temperatures of the layer. The mass per unit area of an element dP is dP/g , so the number of molecules of molecule m is

$$dn_m = N q_m dP / g [M_d + q^w M_w] \quad (\text{A.14})$$

where N is Avogadro's number, q_m is the volume mixing ratio of molecule m , defined as the ratio to the number of molecules of dry air, M_d and M_w are the molar masses of dry air and water, and q^w is the mixing ratio of water vapor. Hence the number of molecules of m in a layer along the line of sight is

$$u_{lm} = \int_{l_{l-1}}^l q_m(P) f(P) dP \quad (\text{A.15})$$

where

$$f(P) = \sec \theta N / g [M_d + q^w M_w] \quad (\text{A.16})$$

is very nearly constant over a layer. Interpolating $\ln(f)$ as well as $\ln(q_m)$ linearly in $\ln(P)$, we obtain integrals that can be evaluated analytically. Putting

$$q_m f = q_{ml-1} f_{l-1} (P / P_{l-1})^{\alpha_l} \quad (\text{A.17})$$

within the layer, where $\alpha_l = \ln(q_{ml} f_l / q_{ml-1} f_{l-1}) / (\zeta_l - \zeta_{l-1})$, we obtain

$$\begin{aligned} u_{lm} &= [q_{ml-1} f_{l-1} P_{l-1} - q_{ml} f_l P_l] / (1 + \alpha_l) \\ &= q_{ml-1} f_{l-1} P_{l-1} (\zeta_l - \zeta_{l-1}) E[(1 + \alpha_l)(\zeta_l - \zeta_{l-1})] \end{aligned} \quad (\text{A.18})$$

where $E(x) = [1 - \exp(-x)]/x$, which will need special evaluation near $x=0$. The first form is simpler, but the second form is needed when $(1 + \alpha_l) \sim 0$. We also require the weighted mean pressure and temperature obtained from

$$u_{lm} \bar{P}_l = - \int_{l_{l-1}} l_{l-1} q_m f P \, dP \quad (\text{A.19})$$

$$u_{lm} \bar{T}_l = - \int_{l_{l-1}} l_{l-1} q_m f T \, dP \quad (\text{A.20})$$

in order to evaluate the optical depth

$$\tau_v = k_v(\bar{P}, \bar{T}) u \quad (\text{A.21})$$

where k_v is the absorption coefficient (cross section) to be interpolated from a tabulation against pressure and temperature. We easily obtain

$$\begin{aligned} u_{lm} \bar{P}_l &= [q_{ml-1} f_{l-1} P_{l-1}^2 - q_{ml} f_l P_l^2] / (2 + \alpha_l) \\ &= q_{ml-1} f_{l-1} P_{l-1}^2 (\zeta_l - \zeta_{l-1}) E[(2 + \alpha_l)(\zeta_l - \zeta_{l-1})] \end{aligned} \quad (\text{A.22})$$

The temperature integral can also be performed algebraically, but leads to slightly more complicated expressions.

For computational efficiency we wish to avoid a two dimensional interpolation in the absorption coefficient tables. The mean pressure is therefore approximated by its value at $\alpha_l = 0$, and the tabulation made at the corresponding set of layer mean pressures, $\bar{P}_l = (P_l + P_{l-1})/2$. This approximation is in error by 1.2% in pressure at $\alpha = < 1$ for a layer thickness of 1 UARS layer, and is quadratic in layer thickness.

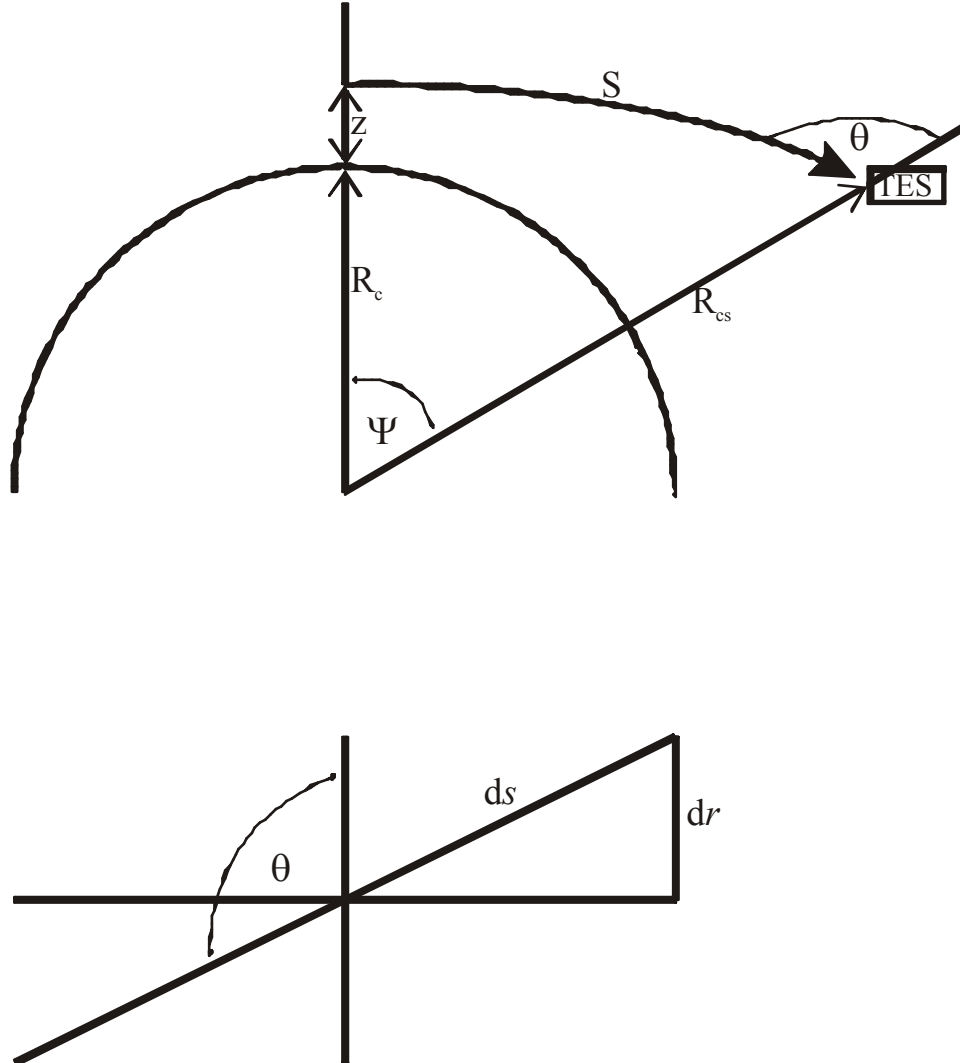
A3.3.1.1.4 Ray Tracing in the Limb Case

To avoid a pressure interpolation in the absorption coefficient table in the forward model, we need to predetermine the layer mean pressures in order to tabulate at the required pressures. Therefore we ray trace forward from a set of tangent points on the full grid (with given pressures) and evaluate the forward model for these rays, rather than tracing from the satellite in a set of directions related to the detector array. The ray trace will provide an angle of incidence at the satellite, so that a quadrature over the field of view of each detector can be carried out.

The use of a pressure grid involves an extra complication, because ray tracing is essentially a geometric procedure, best carried out in height coordinates, while the state vector is defined in pressure coordinates. In the case when horizontal homogeneity is assumed, the approach is relatively straightforward, following the principles of the method used in Kneizys *et al.* (1983). The quantities required from the ray trace are the angle of the ray at the satellite, and the pressure

as a function of distance along the ray, so that path integrals such as $\int q \rho \, ds$, $\int q \rho P \, ds$, and $\int \rho T \, ds$ can be evaluated for each layer.

Figure A-2: Propagation of a refracted ray through the limb



First we use the hydrostatic equation to obtain the heights z_k of the pressure levels for the full grid. These will not be equally spaced in height. We then trace a ray from each z_k as tangent height to the altitude of the satellite, relative to the center of curvature of the geoid. See Figure A-2 to define the terminology. For the refracted ray in the horizontally homogeneous case, the zenith angle of the ray at any altitude can be obtained from Snell's law:

$$n(r)r \sin \theta(r) = r_m \quad (\text{A.23})$$

where $r = z + R_c$ and $r_g = n(r_i)r_t = R_{cs} \sin\theta_s$, is a constant for the ray, the geometric tangent radius or the *impact parameter*. Using

$$dr = \cos\theta \, ds \quad (\text{A.24})$$

we obtain

$$ds = (1 - r_g^2/n^2 r^2)^{-1/2} \, dr \quad (\text{A.25})$$

which cannot easily be integrated numerically to obtain $s(r)$ because of the singularity at the tangent point. However by changing the variable of integration from r to $x = r \cos\theta$ we can obtain

$$ds = dx/[1 - \gamma(r) \sin^2\theta(r)] \quad (\text{A.26})$$

where $\gamma = -(r/n) \partial n / \partial r$, a positive quantity, is an explicit function of r , as is $\sin\theta$. The coordinate x has the property that in the absence of refraction, $x = s$. To integrated over each full grid layer, we choose a set of quadrature points x_l within the layer, and use e.g. the trapezium rule:

$$\Delta s = \sum_i (x_i - x_{i-1}) (1/(1 - \gamma_i \sin^2\theta_i) + 1/(1 - \gamma_{i-1} \sin^2\theta_{i-1}))/2 \quad (\text{A.27})$$

or some higher order integration rule. Note that it is not straightforward to find the altitudes of a set of points equally spaced in x because $x^2 = r^2 - r_g^2/n^2(r)$ cannot be explicitly inverted to give $r(x)$, even though x can be evaluated at any given value of r . Either $r^2(x) = x^2 + r_g^2/n^2(r)$ must be evaluated iteratively, or points chosen in r^2 to make them approximately evenly spaced in x .

The refractive index of air is given in section A3.3.1.1.8 as an experimentally fitted function of pressure, temperature and water vapor. However it is close to being of the form $n = 1 + \alpha \rho(r)$, where α is a constant, so that within each narrow layer, such as the full grid layer, it may be reasonably fitted to the form

$$n = 1 + \alpha \rho_0 \exp(-r/H_n) \quad (\text{A.28})$$

so that we can write

$$\partial n / \partial r = -(n - 1) / H_n \quad (\text{A.29})$$

where H_n is the scale height of refractivity, $n-1$, within the layer.

A3.3.1.1.5 Path Integrals for the Limb Case

The absorber amount of molecule m in a sublayer, $\Delta u_m = \int q_m \rho \, ds$ can be evaluated in the same way as Δs by integrating with respect to x using the trapezium (or other) rule:

$$\Delta u_m = \sum_l (x_l - x_{l-1})(q_{lm}\rho_l/(1-\gamma_l\sin^2\theta_l) + q_{ml-1}\rho_{l-1}/(1-\gamma_{l-1}\sin^2\theta_{l-1}))/2 \quad (\text{A.30})$$

The effective pressure for a full grid layer is defined by

$$\bar{P} = \int \rho P \, ds / \int \rho \, ds \quad (\text{A.31})$$

where the two integrals are evaluated as sums over sublayers within the full grid layer, the elements of the sums being

$$\int \rho P \, ds = \Delta(uP) = \sum_i (x_i - x_{i-1})(P_i\rho_i/(1-\gamma_i\sin^2\theta_i) + P_{i-1}\rho_{i-1}/(1-\gamma_{i-1}\sin^2\theta_{i-1}))/2 \quad (\text{A.32})$$

and

$$\int \rho \, ds = \Delta u = \sum_i (x_i - x_{i-1})(\rho_i/(1-\gamma_i\sin^2\theta_i) + \rho_{i-1}/(1-\gamma_{i-1}\sin^2\theta_{i-1}))/2 \quad (\text{A.33})$$

The integral over the lowest sublayers (close to the tangent point) should be evaluated using a quadratic rule.

The effective temperature for a full grid layer is defined by

$$\bar{T} = \int \rho T \, ds / \int \rho \, ds \quad (\text{A.34})$$

in a similar way to the effective pressure. The elements of the sum for the numerator are

$$\Delta(uT) = \sum_i (x_i - x_{i-1})(T_i\rho_i/(1-\gamma_i\sin^2\theta_i) + T_{i-1}\rho_{i-1}/(1-\gamma_{i-1}\sin^2\theta_{i-1}))/2 \quad (\text{A.35})$$

Again, the integral over the lowest sublayers should be evaluated using a quadratic rule.

A3.3.1.1.6 Ray tracing in the Inhomogeneous Limb Case.

It is marginal whether the change in the refracted path due to horizontal inhomogeneities is significant. In the worst case, the slope of a pressure surface of 0.001, corresponding to a geostrophic wind of $100 \, \text{m s}^{-1}$, gives an error in tangent height at mid troposphere of order 40 m, or about 0.5% in pressure or density. Nevertheless we give the following analysis to describe a possible approach, should it be needed on further investigation.

In the general case the refraction equations do not have an explicit solution expressible as integrals, unlike the horizontally homogeneous case. A set of coupled ordinary differential equations can be derived, relating $r(s)$, $\theta(s)$ and $\psi(s)$:

$$d(\theta+\psi)/ds = -\sin\theta/n \, (\partial n/\partial r)_\psi + (\cos\theta/rn)(\partial n/\partial \psi)_r \quad (\text{A.36})$$

$$dr/ds = \cos\theta \quad (A.37)$$

$$d\psi/ds = \sin\theta/r \quad (A.38)$$

where ψ is the angle at the center of curvature relative to the instrument. The first equation states that the curvature of the ray is equal to the fractional gradient of the refractive index normal to the ray. The others are simple geometry. We can use (A.36) and (A.38) to obtain:

$$d\theta/ds = -\sin\theta[1/r + 1/n (\partial n/\partial r)_\psi] + (\cos\theta/rn)(\partial n/\partial \psi)_r \quad (A.39)$$

Equations (A.36), (A.37) and (A.38) can be integrated by any standard differential equation solver such as Runge-Kutta to give $r(s)$, $\theta(s)$ and $\psi(s)$.

The boundary conditions cause difficulties, however. A single ray must pass through the instrument at a known location, and have a tangent point at a given pressure level:

- (i) at $s = 0$, $\psi(0) = 0$ and $r(0) = R_{cs}$
- (ii) at $r=r(\zeta_i)$, $\cot\theta = - (1/r)(\partial r/\partial \psi)_\zeta$, i.e the slope of pressure surface ζ_i

where $\zeta = -\ln(P/P_0)$. Here I have put the origins of ψ and s at the instrument for convenience. We do not know before the ray trace where ψ of the tangent point is relative to the satellite. (This does not matter in the case of the horizontally homogeneous atmosphere.) Therefore we must solve the problem iteratively by either:

- (a) finding the value of ψ at the tangent point for which the ray passes through the instrument, or
- (b) finding the scan angle θ_s at the satellite which gives a tangent point at the right pressure level

To locate the tangent point relative to the satellite, it is most convenient to locate the origin of s at the tangent point and the origin of ψ at the instrument. The initial conditions are, at the tangent point

$$(i) \ s = 0 \quad (ii) \ r = r_t \quad (iii) \ \psi = \psi_t \quad (iv) \ \cot\theta = -(1/r)(\partial r/\partial \psi)_\zeta.$$

Integrate forward from the tangent point until the ray reaches satellite altitude R_{cs} . The ray will miss the instrument by an amount $\psi(R_{cs})$. This quantity is then subtracted from ψ_t for the next iteration. If there were no line of sight gradients, we would need to go no further, but one more iteration will probably be necessary for convergence.

The temperature, water and (hence) the refractive index are specified vertically on the full grid, and horizontally at some set of values of ψ . Use the hydrostatic equation to find r on this same grid. Then the table can be used to find the partial derivatives $(\partial n/\partial r)_\psi$, $(\partial n/\partial \psi)_r$ and $(\partial r/\partial \psi)_\zeta$ where they are required.

There is the extra complication that we want to find quadrature points along the rays lying on the full grid. We are at liberty to choose the quadrature points for the integration so we will change

them as we iterate so that a subset ends up lying on the pressure grid. The suggested process is as follows, for each full grid level within the range seen by the instrument:

Repeat:

- Select a set of quadrature points in s :
- First time round, use $s = ih$, $i=0,1..$ for some constant spacing h .
- Subsequent times we will have a reasonable guess at the ray path, so use the tangent point, plus points where the ray intersects the full grid (inverse interpolate in $\zeta(s)$), subdividing sections so that no interval is longer than h .
- Adjust the initial condition ψ_t
- Integrate forward & backward through the atmosphere to give $r(s)$, $\theta(s)$ and $\psi(s)$.
- Use a straight line ray from just outside the atmosphere where $n=1$ to the satellite altitude to calculate the angle ψ_s by which the ray misses the instrument
- Evaluate $\zeta(s)$ at each quadrature point (use r , ψ to interpolate in the 2-D profile table). until converged (fixed number of times, probably 3 or 4)

Carry out the path integrals using the same quadrature points and e.g. Simpsons rule.

The fixed number of iterations is required so that we safely can do a numerical perturbation of the ray trace for the Jacobian calculation.

A reasonable initial value for ψ_t can be obtained by starting with the highest tangent point required, initialized with the geometric (unrefracted) value, and work downwards, each time using the final value for the previous level as the initial value for the current level.

We should probably check for pathological circumstances such as the ray being refracted below the tangent level, by at least checking whether $r < r_t$! This applies to the homogeneous case too.

The alternative approach of finding the scan angle θ_s at the satellite which gives a tangent point at the right pressure level turns out to be more complicated, and not worth pursuing:

A3.3.1.1.7 The gas equation for air

The gas equation for air is given by Ciddor [1996] as

$$\rho = \frac{M_{dry}}{R^*T} p \cdot \frac{\left[1 - X_{H_2O} \left(1 - \frac{M_{H_2O}}{M_{dry}} \right) \right]}{Y}, \quad (A.40)$$

where $R^* = 8.31451 \text{ J mole}^{-1} \text{ K}^{-1}$, the universal gas constant;

$$M_{dry} = [28.9635 + 12.011 \cdot 10^{-6} (X_{CO_2} - 400)] \cdot 10^{-3} \text{ kg/mole};$$

$$X_{CO_2} = 1.5202 \cdot q_{CO_2};$$

$$M_{H_2O} = 0.018015 \text{ kg/mole};$$

$$X_{H_2O} = 0.6223 \cdot q_{H_2O}; \text{ and}$$

the compressibility factor Y is given by

$$Y = 1 - (P/T)[a_0 + a_1 t + a_2 t^2 + (b_0 + b_1 t)X_{H_2O} + (c_0 + c_1 t)X_{H_2O}^2] + (P/T)^2(d + eX_{H_2O}^2)$$

where

$$a_0 = 1.58123e^{-6}$$

$$a_1 = 2.9331e^{-8}$$

$$a_2 = 1.1043e^{-10}$$

$$b_0 = 5.707e^{-6}$$

$$b_1 = 2.051e^{-8}$$

$$c_0 = 1.9898e^{-4}$$

$$c_1 = 2.376e^{-6}$$

$$d = 1.83e^{-11}$$

$$e = -0.765e^{-8}$$

$$\text{and } t = T - 273.15$$

A3.3.1.1.8 Refractive index of air

The index of refraction of air (n) depends on frequency (ν), pressure (P), temperature (T) and water vapor amount (partial pressure P_{H_2O}). Since the original Edlén equation was published in the early 1960's [Edlén, 1966], many revised empirical formulas have been published based on the new measurements. We use a revision of Edlén by Birch and Downs [1993 and 1994]:

$$\begin{aligned} n &= n_{tp} - f \cdot (a_9 - a_{10} \nu^2) \cdot 10^{-10}; \\ n_{tp} - 1 &= \frac{P(n_s - 1)}{a_5} \cdot \frac{[1 + 10^{-8}(a_6 - a_7 t)P]}{(1 + a_8 t)}; \text{ and} \\ (n_s - 1) \cdot 10^{-8} &= a_0 + a_1 \cdot (a_2 - \nu^2)^{-1} + a_3 (a_4 - \nu^2)^{-1}; \end{aligned} \tag{A.41}$$

where a_0 to a_{10} are constants ($a_0 = 8342.54$; $a_1 = 2406147.0$; $a_2 = 130.0$; $a_3 = 15998.0$; $a_4 = 38.9$; $a_5 = 96095.43$; $a_6 = 0.601$; $a_7 = 0.00972$; $a_8 = 0.003661$; $a_9 = 3.7345$; $a_{10} = 0.0401$;), ν is frequency in mm^{-1} , P is pressure in Pa, t is temperature in $^{\circ}\text{C}$ ($t = T - 273.15$), and f is the partial pressure of water vapor.

Although the above formula was derived from measurements of visible and near infrared region, other measurements suggest that it could be extrapolated to the infrared region [Coleman *et al.*, U.S. NBS, "Table of Wavenumbers", 1960]. Note that frequency (ν) only has a secondary effect on n , so that the ray-trace step simply uses the averaged frequency for the forward model spectrum range in the calculation.

A3.3.1.5: Non-LTE

The single-line volumetric absorption κ_ν and local thermal radiance R_ν is given by

$$\kappa_\nu = \frac{h\nu}{4} \bar{B} (g_u n_\ell - g_\ell n_u) \phi_\nu \quad (\text{A.42})$$

and

$$R_\nu = \frac{h^2 \nu^4}{2\pi c^2} g_\ell n_u \chi_\nu, \quad (\text{A.43})$$

where

$$\chi_\nu = \phi_\nu e^{-h(\nu - \nu_o)/kT}, \quad (\text{A.44})$$

where n_ℓ and n_u are the number density populations of the lower and upper V-R states and the constant integers g_ℓ and g_u , are the respective single state degeneracy factors.

This result is a general one for a two-level system. The lineshapes, χ_ν and ϕ_ν , are functions of the bulk thermodynamic quantities such as pressure, temperature, plus individual gas densities which can separately influence the lineshapes. The populations are given by the Boltzman distribution only under conditions of local thermodynamic equilibrium. In the presence of a strong radiation field, or under conditions for which the relaxation rates are slow with respect to physical processes influencing the state populations, the upper and lower state populations are not simply related through Boltzmann factors associated with a characteristic temperature for the system and the source function for the radiance is no longer given by the Planck function.

In the present case for TES observations, several assumptions can be made which significantly simplify the Non-LTE problem: (1) the relevant transitions occur at low pressure so that the Doppler shape is dominant with the line shape for emission and absorption being the same; (2) the system is in translational equilibrium with a characteristic kinetic temperature (affects only the Doppler width); and (3) the system is in rotational equilibrium with a characteristic rotational temperature. In the present formulation, the Non-LTE radiative transfer is developed as an extension of the LTE radiative transfer minimizing complexity and computational cost. The Non-LTE vibrational state population variables can be used to relate the Non-LTE single-line absorption and radiance to the same quantities calculated for an atmosphere in equilibrium at the characteristic temperature \bar{T} . The relationship between non-equilibrium and equilibrium radiative properties for a single line can be summarized by

$$\kappa_\nu = \left[\frac{g_u n_\ell - g_\ell n_u}{g_u n_\ell^e - g_\ell n_u^e} \right] \kappa_\nu^e \quad (\text{A.45})$$

and

$$R_v = \frac{n_u}{n_u^e} R_v^e, \quad (\text{A.46})$$

which can also be written in terms of the Planck function as

$$R_v = \frac{n_u}{n_u^e} B_v(\bar{T}) K_v^e. \quad (\text{A.47})$$

The superscript e denotes the equilibrium values of the respective quantities.

The ratios of non-LTE vibrational populations to their equilibrium values are given as enhancement (or depletion) ratios,

$$r_\ell = \frac{n_\ell}{n_\ell^e} \quad \text{and} \quad r_u = \frac{n_u}{n_u^e}. \quad (\text{A.48})$$

The single-line contributions to K_v and C_v due to a transition with wavenumber value ν_o can be expressed simply in terms of these ratios according to

$$K_v = \left[\frac{r_\ell - r_u \Delta}{1 - \Delta} \right] K_v^e \quad (\text{A.49})$$

and

$$C_v = \left[\frac{r_\ell - r_u}{1 - \Delta} \right] K_v^e \quad (\text{A.50})$$

where Δ is the Boltzman factor,

$$\Delta = \frac{g_\ell n_u^e}{g_u n_\ell^e} = e^{-h\nu_o/k\bar{T}}. \quad (\text{A.51})$$

The factors in brackets can be viewed as Non-LTE line strength correction factors. The functions, K_v and C_v , are obtained from the equilibrium values of the spectral absorption coefficients tabulated for individual vibrational states of a given molecular species. The quantities required for the calculation are r_ℓ , r_u and ν_o for each Non-LTE vibrational state.

The complete solution of the radiative transfer equation for a homogeneous layer with column amount, u , is given by

$$L_v = L_v^o e^{-K_v u} + B_v(\bar{T}) \left[1 - \frac{C_v}{K_v} \right] [1 - e^{-K_v u}] \quad (\text{A.52})$$

where L_v^o is the radiation at the path boundary. The effect of solving the non-equilibrium problem for a homogeneous layer is effectively to modify the line strengths (equilibrium absorption coefficients) contributing to the local absorption coefficient K_v , and to replace the Planck function B_v by the high resolution function $B_v(\bar{T})[1 - C_v / K_v]$.

A3.3.1.5.1:Non-LTE:NO Example

Non-LTE will occur under conditions for which relaxation rates are slow with respect to physical processes influencing the state populations. Initial testing and sensitivity studies using TES LBLRTM are performed using the method outline above in section A3.3.1.5. The Non-LTE vibrational temperatures for NO at $v=1$ state were obtained from Funke and Puertas [2000] Non-LTE model (refer to Figure A-3 and Figure A-4), and the mixing ratio from the AFGL NO profile [Anderson, et. al, 1986] (refer to Figure A-5). The results from the Non-LTE model for NO($v \leq 2, J, S$) in Figure A-3 show that there is significant departure from LTE for NO($v \geq 1$) in the stratosphere daytime as low as 15 km due to the production by NO₂ photolysis. The issue of rotational and spin distributions of NO($v=1,2$) shown to be in Non-LTE above ~110 km must also be evaluated.

Figure A-3: NO kinetic, $v=1$, and $v=2$ vibrational temperatures in the daytime. Digitized from Funke and Puertas [2000].

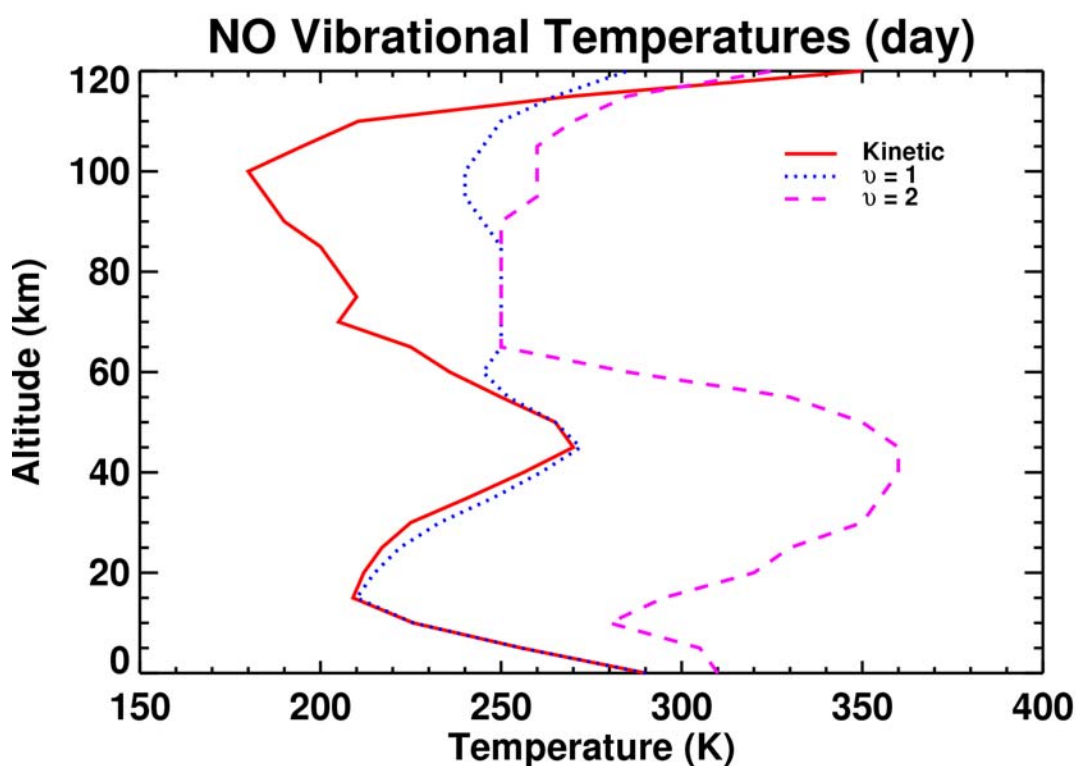


Figure A-4: NO kinetic, $v=1$, and $v=2$ vibrational temperatures in the nighttime. Digitized from Funke and Puertas [2000].

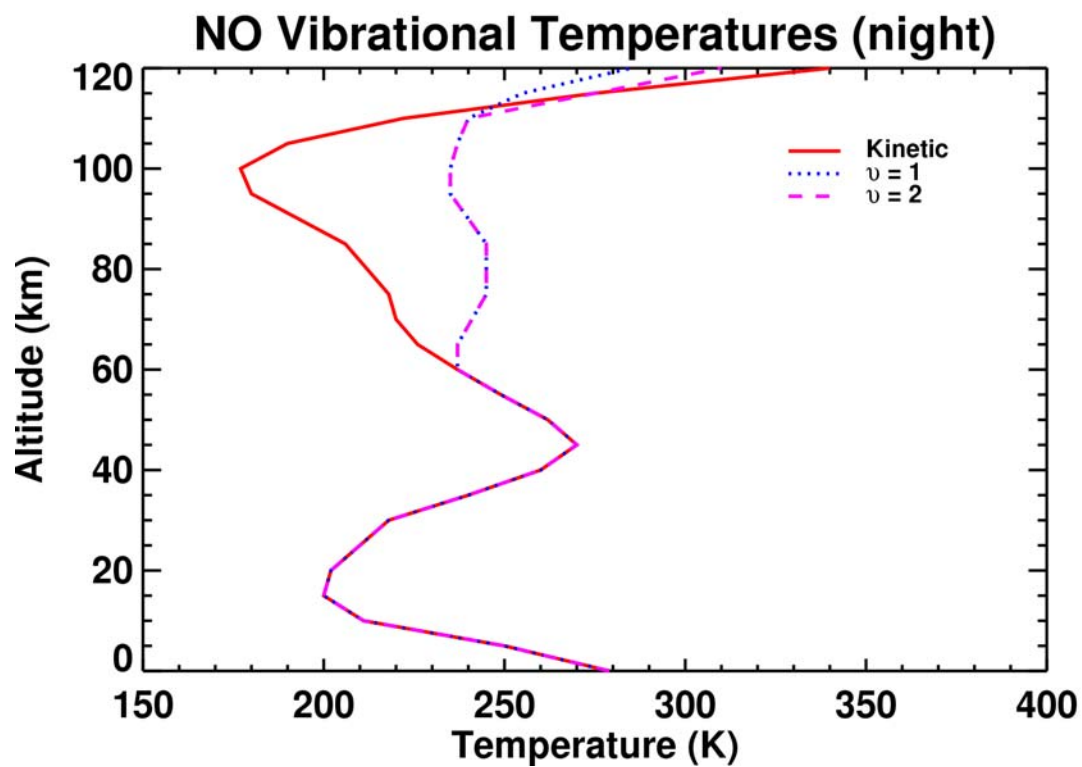


Figure A-5: US standard atmosphere profiles of NO mixing ratio and temperature [Anderson et. al., 1986].

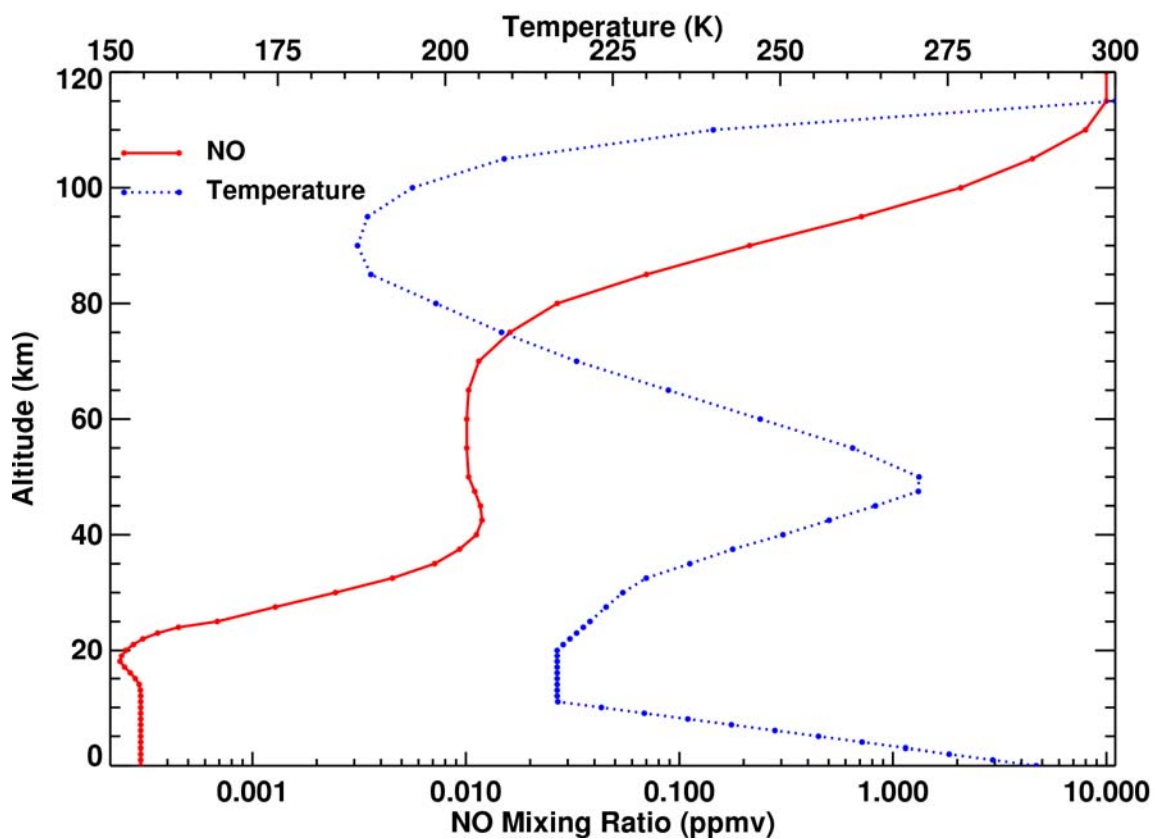


Figure A-6: TES LBLRTM computed spectra of NO under Non-LTE ($v=1$) daytime conditions for a limb path with a tangent height of 15 km. The results are plotted in both brightness temperature (top) and radiance (bottom).

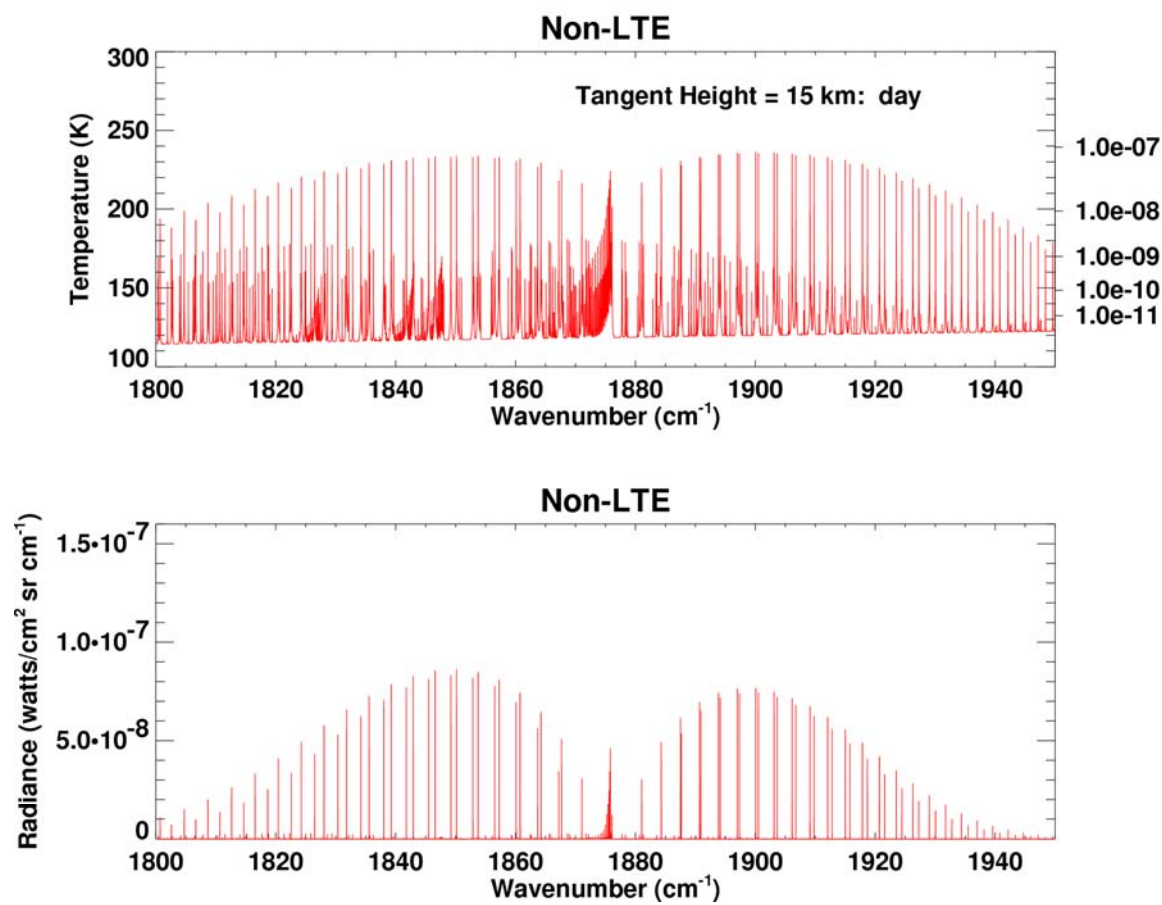
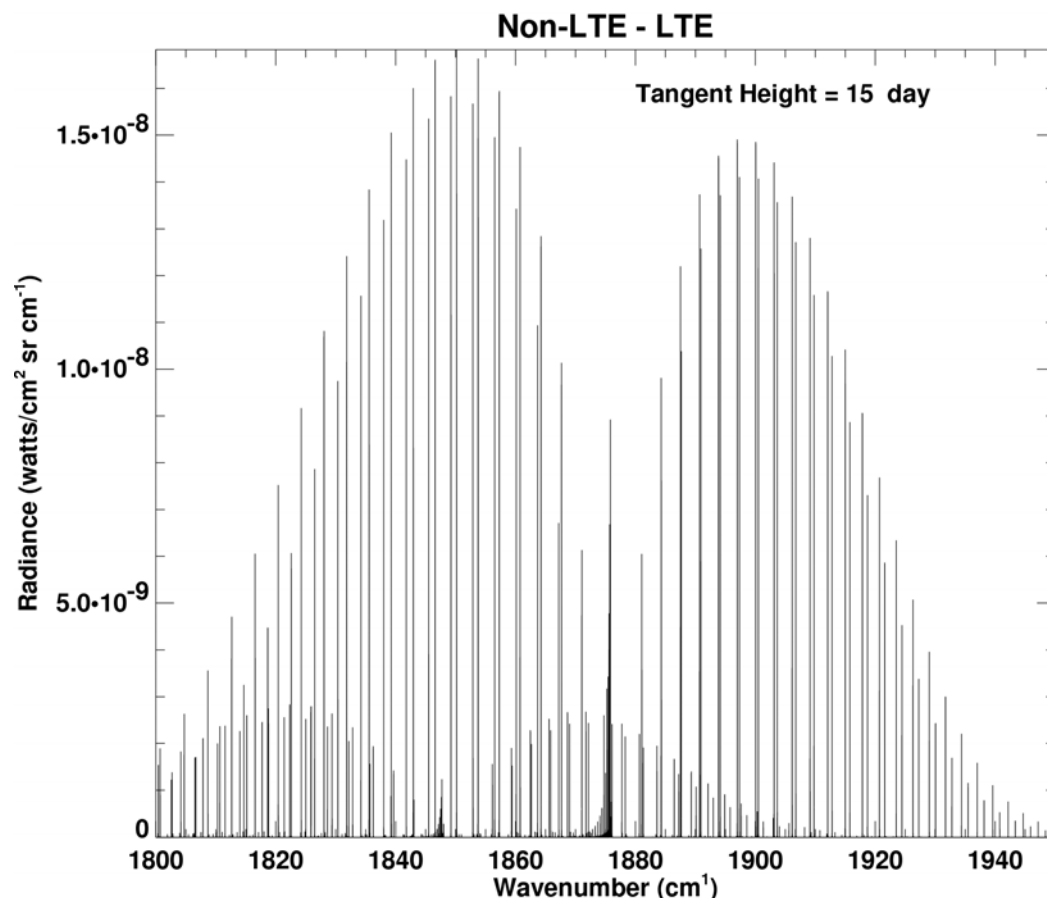


Figure A-7: Difference plot between TES LBLRTM calculated radiances under Non-LTE ($v=1$) and LTE (kinetic temperature) conditions.



NO radiances have been computed under both LTE and Non-LTE($v=1$) conditions for paths with tangent heights of 15 and 30 km during both day and night. Figure A-6 is the TES LBLRTM computed spectra of NO under Non-LTE daytime conditions for a tangent height of 15 km using inputs given in Figure A-3 and Figure A-5. The differences between the NO Non-LTE and LTE for this example are shown in Figure A-7 and have a maximum value of $8.4 \times 10^{-8} \text{ W/cm}^2 \text{ sr cm}^{-1}$. This difference corresponds to a percent maximum relative difference of $\sim 20\%$. These differences neglect the effect of thermospheric rotational/spin Non-LTE. Similar calculations were performed for a tangent height of 30 km under both day and night conditions and summarized in Table A-1. This differences in radiation due to Non-LTE effects in the stratosphere and thermosphere will have a significant impact on TES tropospheric NO retrievals and will be taken into consideration in the retrieval process as outlined in Section 3.3.1.5.

Table A-1: Summary of results for Non-LTE vs. LTE TES LBLRTM calculations.

Day/Night	Tangent Height (km)	Maximum Non-LTE NO Radiance ($\text{W/cm}^2 \text{ sr cm}^{-1}$)	Non-LTE - LTE Radiance ($\text{W/cm}^2 \text{ sr cm}^{-1}$)	Maximum Relative Difference (%)
DAY	30	1.27×10^{-7}	2.65×10^{-8}	21
DAY	15	8.4×10^{-8}	1.7×10^{-8}	20
NIGHT	30	8.5×10^{-8}	9.6×10^{-10}	1.1
NIGHT	15	5.9×10^{-8}	8.8×10^{-10}	1.5

A3.3.2.2: Map of Earth Surface Composition

Global Land Cover Characteristics Data Base

This appendix describes an existing source of global land cover maps with 1 km resolution and a choice of land classification schemes. This database was generated by the U.S. Geological Survey (USGS) Earth Resources Observation System (EROS) Data Center, the University of Nebraska-Lincoln (UNL) and the Joint Research Centre of the European Commission and is described in more detail at: <http://edcwww.cr.usgs.gov/landdaac/glcc/glcc.html>. Their maps are derived primarily from 1 km resolution composites of normalized difference vegetation index (NDVI) data from the Advanced Very High Resolution Radiometer (AVHRR) for the 12 month period of April 1992-March 1993. (NDVI values are the difference divided by the sum of the near infrared (channel 2) and visible (channel 1) reflectance values, after calibration and atmospheric corrections). The strategy for global land cover characterization is given in Loveland *et al* [1991, 1995] and Brown *et al* [1993] and an AVHRR data quality evaluation is described in Zhu and Yang [1996]. The global land cover maps are available in 6 different classifications schemes with a range of 10 to 94 land cover types. These schemes are optimized to provide relevant information for research in areas such as atmospheric general circulation models and land use studies. Three of these classification schemes include urban/built-up areas as a land cover type, a useful distinction for our purposes. These are the Global Ecosystems classification (94 classes), Olson [1994 a&b]; the USGS Land Use/Land Cover System (24 classes), Anderson *et al* [1976]; and the International Geosphere Biosphere Programme (IGBP) Land Cover Classification (17 classes), Belward [1996]. Although we should not preclude the use of the more detailed Global Ecosystems classification, the USGS Land Use/Land Cover system (listed below) has been chosen for the initial algorithm development. The IGBP scheme, although simpler, was not chosen because there were no classes to distinguish moist vs. dry vegetation, an important distinction because of significant spectral IR reflectance differences. None of the land cover classifications in this database distinguished ice from snow, and an additional database may be needed for these areas.

Table A-2: USGS Land Use/Land Cover System Legend and Assignment of Material Type from the ASTER Spectral Library (<http://speclib.jpl.nasa.gov/>)

Value	Code	Description	Default material types to use for surface emissivity
1	100	Urban and Built-Up Land	construction asphalt, grass, deciduous
2	211	Dryland Cropland and Pasture	dry grass
3	212	Irrigated Cropland and Pasture	Grass
4	213	Mixed Dryland/Irrigated Cropland and Pasture	grass, dry grass
5	280	Cropland/Grassland Mosaic	grass, dry grass
6	290	Cropland/Woodland Mosaic	grass, deciduous, conifer
7	311	Grassland	Grass
8	321	Shrubland	Deciduous
9	330	Mixed Shrubland/Grassland	Deciduous, grass
10	332	Savanna	dry grass
11	411	Deciduous Broadleaf Forest	Deciduous
12	412	Deciduous Needleleaf Forest	Conifer
13	421	Evergreen Broadleaf Forest	Conifer
14	422	Evergreen Needleleaf Forest	Conifer
15	430	Mixed Forest	Deciduous, conifer
16	500	Water Bodies	fresh or salt water
17	620	Herbaceous Wetland	Conifer
18	610	Wooded Wetland	Conifer
19	770	Barren or Sparsely Vegetated	brown gravelly sandy loam
20	820	Herbaceous Tundra	Deciduous
21	810	Wooded Tundra	Conifer
22	850	Mixed Tundra	Deciduous, conifer
23	830	Bare Ground Tundra	dry grass
24	900	Snow or Ice	coarse granular snow

A3.3.3 Radiative Transfer for Clouds and Aerosols

A3.3.3 Radiative Transfer for Clouds and Aerosols

Aerosols and clouds (scattering materials) have the potential to impact TES measurements. This appendix will describe the overall strategy for dealing with scattering materials and refer the reader to the relevant sections in the ATBD.

The first step in dealing with scattering materials is to identify measurements that have been impacted. We will use the framework of sorting the data into cases of no clouds, broken or highly inhomogeneous clouds, optically thick clouds, and optically thin clouds. The basic strategy is to examine the brightness temperatures in the atmospheric window regions and use the values and variability of the values to classify the observations. This is discussed in detail in sections 3.5.5 and 3.5.6, pixel categorization.

Target scenes that are categorized as being free of clouds can be processed easily. If broken or highly inhomogeneous clouds are present, the target scene will be excluded from further processing. In the case of an optically thick cloud in the limb, detectors at and below the cloud will be excluded from further analysis. Light scattered into the field of view may need to be considered (see section 3.3.3.2). In nadir views, the cloud will be treated as the surface.

Cases with optically thin clouds in the nadir may be handled with gray body extinction cross sections. This is discussed in greater detail in section 3.3.3. Due to the horizontal inhomogeneity of clouds, attempting to include optically thin clouds in the limb is not recommended.

A3.3.8.1: Line-by-Line Spectral Parameters

The line-by-line portion of the TES spectroscopic database contains transitions for individual infrared active molecular species and their isotopomers within the spectral range defined by the TES nadir and limb observations. The numbering of the species and format for the parameters are currently the same as in the HITRAN database. The HITRAN parameters are available through the internet or via an ftp site at the Smithsonian Astrophysical Observatory (<http://www.hitran.com>). The parameters and the contents of the HITRAN spectral parameters database were last reviewed for the 1996 HITRAN edition [Rothman et al., 1998]. Since that time, there have been significant improvements for some species. Here we describe the current status, updates, and known limitations of the current HITRAN parameters for the molecules and spectral regions of importance to TES. Laboratory work in progress, and published results not incorporated in HITRAN are also discussed. As was done for the ATMOS project [Brown et al., 1996], a TES spectroscopic database will be maintained to satisfy the specific needs of the TES project including all available sources (e.g. HITRAN, GEISA [Husson et al., 1999; 2000]). Status of current spectroscopy and anticipated needs proceeds on a molecule-by-molecule basis, with the description for each molecule in ascending wavenumber

H₂O (molecule 1)

The significant deficiencies for water vapor on the HITRAN 1996 compilation in the thermal IR spectral region covered by TES have been greatly reduced as a result of the work of Toth (e.g. Toth [1998]). The major update includes the positions, intensities, air-broadening coefficients, self-broadening coefficients, and pressure-induced shifts and covers 500-2820 cm⁻¹. Some transitions were found missing and were added from HITRAN 1996, so the update is not complete.

As was done for the ATMOS compilation [Brown et al., 1996], TES will treat HDO and a separate molecular species because of the large fractionation effects of HDO with respect to H₂O [e.g., Moyer et al. 1996]. The current database does not include the updated positions and

intensities of the HD¹⁶O ν_2 band derived by Flaud et al. [1986] and the more recent ν_2 HD¹⁶O, HD¹⁷O, and HD¹⁸O position and intensity analysis results of Toth [1993]. The parameters of Flaud et al. [1986] have been regenerated (J.-M. Flaud, private communication) and are now available to the TES project with approximate air-broadened widths (C. P. Rinsland, private communication, 1998). Air-broadened pressure shifts are set to zero.

CO₂ (molecule 2)

HITRAN infrared intensities require updating with a self-consistent calculation of energy levels including new measurements of positions, intensities, air-broadening width and air-broadened shift coefficients measured at Kitt Peak by the NASA Langley group in several spectral regions [Malathy Devi et al., 1998a,b,c] and new measurements in the 4500- to 8000 cm⁻¹ region by Miller [2001]. The 1996 HITRAN compilation parameters were based on a global least-squares fit of the energy levels of carbon dioxide [Rothman et al., 1998]. The new update should include the air-broadened pressure-shift coefficient measurements in the 10 μ m laser bands, which have been demonstrated to be detectable in ground-based solar spectra [Malathy Devi et al., 1998c].

The update is of critical importance because of the use of CO₂ for temperature sounding by TES. Additional CO₂ measurements of intensities, broadening, and shift coefficients in the 4.2-4.5 μ m region (¹²C¹⁶O₂, ¹³C¹⁶O₂, and ¹³C¹⁶O¹⁸O) and in the 10 μ m laser bands are soon to be reported by the NASA Langley group (e.g. Malathy Devi et al. 2002]. The results were derived from room temperature 0.01-cm⁻¹ resolution laboratory spectra recorded at Kitt Peak. The spectroscopy of CO₂ in the infrared was reviewed by Malathy Devi et al. [1997].

O₃ (molecule 3)

Simultaneous pure-rotation and 10- μ m measurements of line intensities are needed to resolve the 3-4% discrepancy between measurements performed at Kitt Peak by the NASA Langley group [Smith et al., 2001] and values obtained at the Deutsches Zentrum für Luft und Raumfahrt (DLR) [Wagner et al., 2000] and at LPMA [Claveau et al., 2001]. The DLR and LPMA measurements are both lower than the Kitt Peak measurements, which are 1% higher than HITRAN 1996 [Rothman et al., 1998]. The Kitt Peak intensities agree with the current HITRAN values within experimental error. Field measurements indicate the current HITRAN values are accurate to better than 5% [Toon et al., 1999, plate 4]. If the 10- μ m O₃ intensities are modified, the intensities in all other IR spectral regions must be scaled by the same factor to retain consistency. The DLR measurements from 16 spectra were at temperatures between 200 and 296 K and air pressures between 0.0 to 40 mbar were also analyzed to determine air-broadening coefficients, which were fitted with an empirical expansion in m and temperature [Wagner et al., 2000]. Those results differ significantly from values predicted by the current HITRAN compilation with important implications for the derivation of tropospheric ozone profiles from the TES nadir and limb-viewing spectra.

Updates of O₃ parameters on the 1996 HITRAN compilation have been summarized [Rinsland et al., 1998a]. Spectra of ¹⁷O-enriched ozone samples recorded at 0.005-cm⁻¹ resolution were analyzed to derive the line positions and intensities for the ν_1 and ν_3 bands of ¹⁶O¹⁷O¹⁶O [Heyart et al., 1992] and ¹⁶O¹⁶O¹⁷O [Heyart et al., 1993]. As described by Rinsland et al. [1998a], these parameters, which were not included on HITRAN 1996 [Rothman et al., 1998] and are still not in that database. A combined list was used to identify isolated lines of the ν_3 bands of ¹⁶O¹⁷O¹⁶O and

$^{16}\text{O}^{16}\text{O}^{17}\text{O}$ in both high resolution ground-based and balloon-borne stratospheric solar absorption spectra. As shown in that work, they are detectable in atmospheric spectra, and hence should be added to the TES database.

Bands of O_3 at 4.7 μm are about one third as strong as those at 10 μm and are important absorbers in the region that will be used to retrieve CO profiles from the TES spectra. The first high-resolution analysis of the $\nu_1 + \nu_3$ bands of $^{16}\text{O}^{16}\text{O}^{18}\text{O}$ and $^{16}\text{O}^{18}\text{O}^{16}\text{O}$ at 4.8 μm was performed by Flaud et al. [1994]. On the basis of that work, isolated lines of both heavy isotopic species were identified in high resolution ground-based solar absorption spectra by Arlander et al. [1994] and Goldman et al. [1998]. Line parameters for the $\nu_1 + \nu_3$ bands of $^{16}\text{O}^{18}\text{O}^{16}\text{O}$ and $^{16}\text{O}^{16}\text{O}^{18}\text{O}$ [Flaud et al., 1994] and $^{16}\text{O}^{17}\text{O}^{16}\text{O}$ and $^{16}\text{O}^{16}\text{O}^{17}\text{O}$ [Perrin et al., 2001] should be added to the TES database. However, users must keep in mind that the corresponding intensities are not really accurate since they were calculated using the transition moments of the main isotopic species $^{16}\text{O}_3$.

Modeling of line mixing may be required for accurate simulations in Q-branch regions. As models suggest non-LTE may occur above 50 km, high vibrationally excited transitions should be added to the database, at least in the 10- μm region.

N_2O (HITRAN molecule 4).

Infrared measurements of positions, intensities, air-broadening coefficients and their temperature dependence, and pressure-shift coefficients obtained by Toth [2000] need to be made available to the public databases in HITRAN format. Additionally, an extensive set of line intensity measurements has been obtained from 4300-5200 cm^{-1} [Daumont et al., 2001], and a linelist has been generated, though not in HITRAN format (J. Vander Auwera, private communication, 2001). There is good agreement with the results of Toth in regions of overlapping intensity data. Line intensities of $^{14}\text{N}_2^{16}\text{O}$ measured in the 10- μm region agree well with those on the HITRAN 1996 [Rothman et al., 1998] and GEISA 1997 [Jacquinet-Husson et al., 1999] line-parameter compilations, except for some disagreements for the 0001-1000 and 0220-0000 bands [Daumont et al., 2001].

CO (HITRAN molecule 5)

The new, self-consistent calculated set of ro-vibrational line intensities [Chackerian and Freedman, 2001] for the large range of vibrational quantum numbers need to replace current values in the public databases. This improvement is needed primarily for the intensities of the lines in the overtone bands.

CH_4 (HITRAN molecule 6)

HITRAN contains a total replacement of the linelist for this molecule as of February 2001 with a four-fold increase in the number of lines. However, at present there is no documentation of the changes.

O_2 (HITRAN molecule 7)

Spectroscopic parameters for both discrete electric quadrupole transitions and the pressure-induced (1-0) band exist on HITRAN 1996 [Rothman et al., 1998]. More precise measurements

of the pressure-induced band (1-0) band have been reported recently by Lugez et al. [1998]. The new results are in good agreement with the earlier less precise measurements of Orlando et al. [1991] on O₂ and O₂/N₂ mixtures and Thibault et al. [1997] on pure O₂.

NO (HITRAN molecule 8)

As noted by Rothman et al. [1998], the total internal partition functions for NO are incorrect in the HITRAN 1996 database due to an error in the nuclear spin statistical weight factors.

NO₂ (HITRAN molecule 9)

Progress in the analysis of NO₂ since the HITRAN 1996 database [Perrin et al., 1998] has been described by Perrin et al. [2000] with a focus on the 6.2 μm region, which contains the strongest band in the infrared, the ν_3 . The updates in that region include new measurements of positions and intensities of isotopic and hot bands. The hot band measurements may be important for modeling of non-LTE effects in the TES spectra of the upper atmosphere.

Dana et al. [1997] have reported self-, N₂-, and O₂-broadening coefficients of NO₂ lines in the $\nu_1 + \nu_3$ band at 3.4 μm . The study found a slight rotational dependence of the broadening coefficients versus N", whereas no significant dependence was observed versus K_a". An empirical relation was derived to compute air-broadening coefficients at 296 K with an uncertainty of about $\pm 10\%$ for values of N" and K_a" less than 40 and 10, respectively. The authors note that for typical lines used for atmospheric applications, the single value reported in earlier editions of the HITRAN database for all lines of all bands of NO₂ can differ by more than 20% from the measured values [Dana et al., 1997]. A preliminary analysis of unpublished spectra of the 1600 cm⁻¹ NO₂ band indicates that the widths of these lines are also too small in the previous HITRAN linelist with tests indicating that the changes produce a 10% increase in the retrieved mixing ratio of NO₂ at 25 km and little effect above 30 km [Sen et al., 1998]. The updated NO₂ parameters are available as a Sept. 2001 update from the HITRAN website.

HNO₃ (HITRAN molecule 12)

Unpublished fits to Mark IV stratospheric balloon spectra with molecular constants derived by Toth (presented as a poster at the 2001 spectroscopic line parameters workshop in San Diego, CA) show improved fits in the region of the overlapping ν_5 , $2\nu_9$ bands at 11 μm . However, even if some progress were achieved recently (J.-M. Flaud, A. Perrin, and J. Orphal, private communication 2001), problems remain in simulating the narrow and very intense 885-cm⁻¹ hot band and other bands throughout the thermal IR. Retrievals from Mark IV balloon spectra indicate that the normalization of intensities in the HITRAN 2000/2001 database are inconsistent for the major bands at 5.7, 7.5, and 11 μm . Accurate and consistent absolute intensity measurements are still needed for all observable bands throughout the IR.

Perrin et al. [1998] have reanalyzed the $\nu_8 + \nu_9$ band at 1205 cm⁻¹ based on a 0.003-cm⁻¹ resolution laboratory spectrum recorded at the University of Denver. As in a recent analysis [Wang et al., 1997], the Hamiltonian for fitting the line positions takes into account the $\Delta K \pm 2$ anharmonic resonance linking the rotational levels of the $\nu_8=1$, $\nu_9=1$ "bright" vibrational state with those of the $\nu_7=1$, $\nu_8=1$ "dark" vibrational state. However, in contrast to previous work, $\nu_8 + \nu_9$ is noted to be a hybrid-type band with clearly identified B-type transitions among those of the strong A-type lines.

The A- and B-type components of the transition moment operator of the $\nu_8 + \nu_9$ band were determined through a least-squares fit of experimental line intensities measured from the spectrum. The new analysis extends the assignments for the $\nu_8 + \nu_9$ band to maximum rotational quantum numbers of $J=74$ and $K_a=49$ as compared to a maximum J value of 57 [Wang et al, 1997].

OCS (HITRAN molecule 19).

A recent study of high-resolution balloon-borne spectra [Goldman et al., 2000] showed that isotopic $^{16}\text{O}^{12}\text{C}^{34}\text{S}$ lines are observable, and well as weak hot band transitions of $\nu_3 + \nu_2 - \nu_2$ of $^{16}\text{O}^{12}\text{C}^{32}\text{S}$. The line positions and intensities for these bands have been already incorporated into the HITRAN database, but the air-broadening coefficients have not been updated to the level known about OCS.

HOCl (HITRAN molecule 21).

The absolute intensities of lines in the ν_2 band need to be updated based on simultaneous measurements in the infrared with a tunable diode laser and the far infrared by a Fourier transform spectrometer [Vander Auwera et al., 2000].

HCN (HITRAN molecule 23).

This molecule is now recognized as an important tracer of biomass burning with emissions that originate primarily in the smoldering phase of combustion [Rinsland et al. 1998b]. Positions and intensities on HITRAN were calculated more than 20 years ago. Air-broadening coefficients are taken as room-temperature N_2 -broadening coefficients measured at 0.06-cm^{-1} resolution over a decade ago [Smith et al., 1984]. A laboratory run at Kitt Peak in November 2001 has been completed to obtain HCN air-, N_2 -, and O_2 -broadening coefficients as a function of temperature for lines in the 2_2 , $2\nu_2$, and ν_1 regions, which are observable with ground-based and space-borne instruments. Hot-band lines are missing in the ν_1 region on the 2001 HITRAN compilation.

HCOOH (HITRAN molecule 25).

Formic acid is ubiquitous in the troposphere and an important tracer of biomass burning emissions. Spectral parameters have been generated for the ν_6 region, which contains the strongest band located in an atmospheric window [Perrin et al., 1999]. This feature is suitable for quantitative analysis based on absorption by the ν_6 band Q branch at 1104.7 cm^{-1} but the feature is overlapped by a temperature-sensitive line of HDO at $1104.87594\text{ cm}^{-1}$, which was missing in earlier versions of HITRAN, but is now included.

C_2H_6 (HITRAN molecule 27).

Recently, assignments, improved positions, intensities, and air-broadening coefficients and their temperature dependence have been derived for the strong and sharp $^p\text{Q}_3$ subbranch of the ν_7 band at 2976.8 cm^{-1} [Pine and Stone; 1996; Rinsland et al., 1998c; Pine and Rinsland, 1998]. This strong and sharp feature is prominent in ground-based solar spectra [Rinsland et al., 1987; Rinsland et al., 1998c] and nearly free of atmospheric interferences. The new results were obtained from analysis of Doppler-limited and sub-Doppler molecular beam laboratory spectra. It may be possible to measure this C_2H_6 feature in the TES nadir view spectra. Also, it should be noted that

the TIPS program provided on the 1996 HITRAN CD ROM does not compute the C₂H₆ total internal partition function correctly.

COF₂ (molecule 29)

Line assignments in the ν_1 band at 1943 cm⁻¹ are incorrect (J.-M. Flaud, private communications, 2001) and have to be fixed.

ClONO₂ (HITRAN molecule 35).

Current HITRAN absorption cross sections for the region of the ν_4 band Q branch at 780.2 cm⁻¹ should be replaced by temperature- and pressure-dependent 0.0009-0.008 cm⁻¹ resolution laboratory spectra measured between 190 and 296 K and 0.3 to 1.0 mbar measured by Birk and Wagner [2000]. Nearly 30 of these laboratory spectra have been analyzed with the JPL GFIT algorithm to generate the set of ClONO₂ “pseudolines” by simultaneously fitting transmission spectra produced from the laboratory absorption coefficient. Retrievals with the Mark IV spectra indicate a more consistent estimation of the stratospheric chlorine budget than earlier sets of parameters (G. C. Toon, private communication, 2001). A spectroscopic analysis of these bands is in progress and, if successful and validated, should be used in the future [Flaud et al., 2001b]. Additional measurements of low temperature absorption cross-sections are needed for the strong 1700-cm⁻¹ band.

Additional species

COCIF (no HITRAN molecule number).

At present, no parameters exist on the HITRAN database for this molecule, which possibly could be detected in lower stratospheric tropical regions from measurements of its ν_1 band near 1800 cm⁻¹.

COCl₂ (no HITRAN molecule number).

The ν_5 band in the 830- to 860-cm⁻¹ region was recently reported from balloon-borne solar occultation spectra. This identification and the occurrence of the strong ν_1 band centered at 1827 cm⁻¹ [Toon et al., 2001] and the availability of limited spectroscopic parameters in both regions indicate a need for further studies to improve quantitative analysis for both bands.

CH₃OH (no HITRAN molecule number).

The 1033-cm⁻¹ CO-stretch ν_8 band of ethanol is a prominent feature in spectra of biomass burning plumes (e.g. Worden et al., [1997]). Spectral features of this band are likely to be an important interference in retrievals of O₃ from TES spectra recorded under such conditions. To our knowledge, no line-by-line parameters are available for this band, though progress is being made on the analysis of all the IR bands [Xu and Lees, 2000].

IR Cross-Sections

The HITRAN compilation includes infrared absorption cross sections for molecules that cannot be reliably modelled by line-by-line methods. They are C₂F₆, CCl₄, CFC-11, CFC-113, CFC-114, CFC-115, CFC-12, CFC-13, CFC-14, ClONO₂, HFC-123, HFC-124, HFC-141B, HFC-

142B, HCFC-21, HCFC-22, HCFC-225, HFC-125, HFC-134, HFC-134a, HFC-143a, HFC-152a, HFC-34, HNO₄, N₂O₅, and SF₆. Some species are included both as line-by-line and absorption cross section files on HITRAN, so care is required to avoid duplication.

Partition Functions

It is important to note that the partition functions supplied by HITRAN have several significant deficiencies as discussed by Goldman *et al.* [1998].

A3.3.8.2: Cross-Section P-T Interpolation Program XSFINT

1. P-T Point outside table of temperature-pressure values

In this case the "distance" away from every point in the table is calculated and compared to find the closest point. The distance calculation is based on linear distance formulas where the pressure is divided by 10 to give similar units in temperature and pressure.

2. P-T Point inside table of temperature-pressure values

This program picks points based on temperature lines where all temperatures within 2 degrees are considered to be on the same temperature line. A temperature line could look like

Temperature	Pressure
216	50.6
214.1	70.8
215.8	100.0

A table of pressures on temperature lines is constructed from which to pick points. There are four basic cases in the interpolate point outside table of temperature values; four points around target; three points around target; two points around target. The new cross-section records interpolated from the above cases are all written to a new cross-section file. The user can also select the points and interpolation method by hand rather than letting the program select the points and interpolation method.

Four points around target

In this case 2 points on the temperature line before and after the target temperature are found where the points surround the target pressure.

216.6,70.5	217.1,90.2 (temp line after)
210.0,80.0 (target point)	
200.1,69.9	201.0,89.9 (temp line before)

The corner pressures must be within 10% of each other (216.6,70.5 with 200.1,69.9 & 217.1,90.2 with 201.0,89.9) or the tightest diagonal line is picked and the 2 point temperature interpolate is activated, otherwise the 4 point interpolate is activated.

Three points around target

In this case either the temperature line above or below the target contains only one point.

216.6,70.5	217.1,90.2 (temp line after)
	210.0,80.0 (target point)
200.1,69.9	(temp line before)

or

	216.6,70.5	217.1,90.2 (temp line after)
	210.0,80.0 (target point)	
	201.0,89.9	(temp line before)

If the target temperature is within 5 degrees of the temperature line with 2 points, then a 2 point pressure interpolate is activated between those two points. If the target temperature is not close enough to the temperature line with two points, then two points are chosen that create a diagonal (200.1,69.9 with 217.1,90.2 or 216.6,70.5 with 201.0,89.9) then the two point temperature interpolate is activated.

Two points around target

In this case one point on the temperature line before and after the target are used. If both points are either greater or smaller in pressure that the target, then the closest in pressure is used as the new point. If one of the two points are within 4% in temperature and 15% in pressure of the target, then that point is used as new point. If both points are within the 4% and 15% then the closest in temperature is used. If none of the above special cases occur then the 2 point temperature interpolate is activated.

Two point Temperature Interpolate

Two point temperature interpolate does a linear interpolate in temperature between the two pressure/temperature cross-section points for each point in the cross-sections.

Two point Pressure Interpolate

Two point pressure interpolate does a log interpolate in pressure between the two pressure/temperature cross-section points for each point in the cross-sections. (Note In the code the two point pressure interpolate is noted as a 3 point interpolate since two point temperature interpolate is noted as a 2 point interpolate)

Four point Interpolate

Four point interpolate does a linear interpolate in temperature between the side pressure/temperature cross-section points, then a log interpolate in pressure between the two new temperature points resulting from the linear temperature interpolate.

XSFINT Source Code

Xsfint has been compiled and tested on roma in /home/goldman/xsctions/interp. The source code for xsfint is all in one FORTRAN90 file called xsfint.F90. It contains two modules and one main code. The main code is at the end of the file, and must be there for it to use the two modules.

The program has code to create plots using NCAR GKS graphics. The graphics code is currently disabled using conditional compilation with #define, #ifdef, #endif. All sections of graphics code are bracketed in #ifdef NCARGKSOUTPUT, #endif NCARGKSOUTPUT. The first line in the source code has a comment line

```
!#define NCARGKSOUTPUT
```

Uncommenting this line, (removing the "!"), activates the graphics code. The source file is named with .F90 instead of .f90 to activate the pre-processor that processes the NCARGKSOUTPUT lines. To compile xsfint, activate f90 as follows

```
f90 -o xsfint xsfint.F90
```

XSFINT Input

The input file format is as follows

line1 -input cross-section filename

line 2 -output cross-section filename

line 3 -target temperature target pressure interpolate select

interpolate select

0 = Automatic pick of points to interpolate and interpolate method

1 = Use the temperature, pressure shown on line 4 to select a record from the cross-section file as the new point. (manual pick nearest point)

2 = Use the temperature, pressure shown on line 4 and 5 to select 2 records from the cross-section file to do a two point temperature interpolate on.

3 = Use the temperature, pressure shown on line 4 and 5 to select 2 records from the cross-section file to do a two point pressure interpolate on.

4 = Use the temperature, pressure shown on line 4, 5, 6 and 7 to select 4 records from the cross-section file to do a four point interpolate on.

Lines to specify manual selections contain

temperature pressure

There can be multiple target points selected in a run, each possibly with different interpolation selectors.

There is an example case on roma in /home/goldman/xsctions/interp and is named cfc22.test.input. It contains

```
../cfc22.xsect (cross-section file to read)
```

```
cfc22.test.output (cross-section file to create)
```

```
220.0 50.0 3 (target 220.0,50.0 manual select points)
```

```
216.0 176.8 (point 1 for 2 point pressure interp)
```

```
216.0 40.9 (point 2 for 2 point pressure interp)
```

```
240.0 300.0 0 (target 240.,300. auto select points & interp)
```

```
226.0 223.0 2 (target 226.0, 223.0 manual select points)
```

```
237.0 270.4 (point 1 for 2 point temperature interp)
```

216.0 176.8 (point 2 for 2 point temperature interp)

Running XSFINT

To run xsfint on the test case on roma type

xsfint <cfc22.test.input >& cfc22.test.output

This reads cfc22.test.input and creates cfc22.new.xsect and cfc22.test.output.

List of files

All files are on ms are in /GOLDMAN/VARANAS/XSEC.JUNE.97 except where noted otherwise.

CCL4

Xsection file - ccl4.tar

Resolution - 0.03 cm⁻¹

Fixed 0.0025 cm⁻¹ Spc file -ccl4.xsect.25

Avg Spc file - ccl4.xsect.avgspc

Table - table.ME0216 in goldman output subdirectory

Number of Files 32

Wavenumber range 750.0100-811.9900 cm⁻¹

CFC11

Xsection file - cfc11.tar

Resolution - 0.01, 0.03 cm⁻¹

Fixed 0.0025 cm⁻¹ Spc file -cfc11.xsect.A.25
cfc11.xsect.B.25

Avg Spc file - cfc11.xsect.avgspc.A
cfc11.xsect.avgspc.B

Table - table.ME0131 (part a) in goldman output subdirectory
table.ME7904 (part b) in goldman output subdirectory

Number of Files 55

Wavenumber range 810.0060-879.9930 cm⁻¹
1050.0000-1119.9930 cm⁻¹

CFC12

Xsection file - cfc12.tar

Resolution - 0.01, 0.02, 0.03 cm⁻¹

Fixed 0.0025 cm⁻¹ Spc file -cfc12.xsect.A.25
cfc12.xsect.B.25

Avg Spc file - cfc12.xsect.avgspc.A
cfc12.xsect.avgspc.B

Table - table.ME8745 (part a) in goldman output subdirectory
table.ME6165 (part b) in goldman output subdirectory

Number of Files 51

Wavenumber range 850.0050-949.9950 cm⁻¹
 1050.0060-1199.9850 cm⁻¹

CFC22

Xsection file - cfc22.tar
 Resolution - 0.03 cm⁻¹
 Fixed 0.0025 cm-1 Spc file -cfc22.xsect.25
 Avg Spc file - cfc22.xsect.avgspc
 Table - table.ME0088 in goldman output subdirectory
 Number of Files 7
 Wavenumber range 760.0300-860.000 cm⁻¹

SF6

Xsection file - sf6.tar
 Resolution - 0.03 cm⁻¹
 Fixed 0.0025 cm-1 Spc file -sf6.xsect.25
 Avg Spc file - sf6.xsect.avgspc
 Table - table.ME0112 in goldman output subdirectory
 Number of Files 7
 Wavenumber range 925.0100-955.000 cm⁻¹

CF4

Xsection file - cfc14.tar
 Resolution - 0.01, 0.03 cm⁻¹
 Fixed 0.0025 cm⁻¹ Spc file -cfc14.xsect
 Avg Spc file - cfc14.xsect.avgspc
 Table - table.ME0132 in goldman output subdirectory
 Number of Files 54
 Wavenumber range 1250.0050-1289.9975 cm⁻¹

A3.4: Analytic Jacobians

The radiance at the satellite in terms of component contributions from the atmosphere and the surface, but neglecting the solar contribution may be written as

$$L_{sat} = L_L^{\uparrow} + \left(\epsilon B(T_{sf}) + \alpha L_0^{\downarrow} \right) T_{0,L} \quad (\text{A.53})$$

where L_L^{\uparrow} is the upwelling radiance contribution of the atmosphere from the surface to the level at the top of the atmosphere (TOA), $T_{0,L}$ is the transmittance of the atmosphere and L_0^{\downarrow} is the downwelling radiance at the surface. For a specularly reflecting surface, L_0^{\downarrow} is calculated for the same zenith angle as L_L^{\uparrow} and α is the appropriate bi-directional reflectance. For a Lambertian surface, L_0^{\downarrow} is calculated at the diffusivity angle, the downwelling radiation scattered by the surface is taken to be isotropic and α is the albedo.

Due to the form of the radiative transfer equation (equation 3.8), the analytic derivative of the radiance at the satellite with a change in parameter x_l at level l , is most expeditiously obtained in terms of associated layer quantities, so that we have

$$\frac{\partial L_{sat}}{\partial x_l} = \sum_j \frac{\partial L_{sat}}{\partial \bar{x}_j} \frac{\partial \bar{x}_j}{\partial x_l} \quad (\text{A.54})$$

in which x_l is an element of the retrieval vector associated with level l and \bar{x}_j is the associated layer quantity for layer j . Note that in general, x may be mixing ratio (log mixing ratio) or temperature in this context.

For the layer quantities, it is useful to separate the jacobian calculation into partial derivatives with respect to layer total optical depth (τ_l) and Planck function (B_l) via the chain rule. Differentiating Equation (A.54), we obtain

$$\frac{\partial L_{sat}}{\partial x_l} = \frac{\partial L_{sat}}{\partial \tau_l} \frac{\partial \tau_l}{\partial x_l} \quad (\text{A.55})$$

for gas species, and

$$\frac{\partial L_{sat}}{\partial \bar{T}_l} = \frac{\partial L_{sat}}{\partial \tau_l} \frac{\partial \tau_l}{\partial \bar{T}_l} + \frac{\partial L_{sat}}{\partial B_l} \frac{\partial B_l}{\partial \bar{T}_l} \quad (\text{A.56})$$

for layer temperature \bar{T}_l .

The next 5 sections of this appendix give (abbreviated) derivations for each of the terms in equations (A.55) and (A.56). This is followed by section A3.4.6, which gives the layer-to-level partials used in equation (A.54), section A3.4.7 where analytic pointing jacobians are derived and finally section A3.4.8 with results of analytic jacobian validation using finite difference jacobian calculations.

A3.4.1 Partial with respect to layer optical depth (OD) $\frac{\partial L_{sat}}{\partial \tau_l}$

Differentiating (A.53), we obtain

$$\frac{\partial L_{sat}}{\partial \tau_l} = \frac{\partial L_L^\uparrow}{\partial \tau_l} + \alpha \frac{\partial L_0^\downarrow}{\partial \tau_l} \tau_{0,L} + \left(\varepsilon B(T_{sfc}) + \alpha L_0^\downarrow \right) \frac{\partial \tau_{0,L}}{\partial \tau_l} \quad (A.57)$$

Since

$$\tau_{0,L} = \prod_{k=0}^L e^{-\tau_k}, \quad \frac{\partial \tau_{0,L}}{\partial \tau_l} = -e^{-\tau_l} \prod_{k \neq l} e^{-\tau_k} \Rightarrow \frac{\partial \tau_{0,L}}{\partial \tau_l} = -\tau_{0,L} \quad (A.58)$$

equation (A.57) becomes

$$\frac{\partial L_{sat}}{\partial \tau_l} = \frac{\partial L_L^\uparrow}{\partial \tau_l} + \left[\alpha \frac{\partial L_0^\downarrow}{\partial \tau_l} - \left(\varepsilon B(T_{sfc}) + \alpha L_0^\downarrow \right) \right] \tau_{0,L} \quad (A.59)$$

where $\varepsilon=0$ and $\alpha=1$ for limb calculations. We now need to evaluate the separate upwelling and downwelling terms.

A3.4.1.1 Downwelling OD partials $\frac{\partial L_0^\downarrow}{\partial \tau_l}$

For any layer l , the downwelling radiance at the corresponding level l is given by

$$L_l^\downarrow = L_{l+1}^\downarrow \tau_l + B(\overline{T_l})(1 - \tau_l) \quad (A.60)$$

Where $L_{l=L}^\downarrow$ is initialized to zero radiance for the top of the atmosphere. Differentiating equation (A.60) we have

$$\frac{\partial L_l^\downarrow}{\partial \tau_l} = \left(B(\overline{T_l}) - L_{l+1}^\downarrow \right) \tau_l \quad (A.61)$$

At any stage in the recursive calculation, we can write the downwelling radiance at level 0, L_0^\downarrow , as the sum of two terms:

$$L_0^\downarrow = L_l^\downarrow \tau_{l,0} + L_{l,0}^\downarrow \quad (A.62)$$

i.e., the downwelling radiance down to level l attenuated by the transmission from level l to level 0 plus the radiance contribution between levels l and 0, (see Figure A-8). Thus

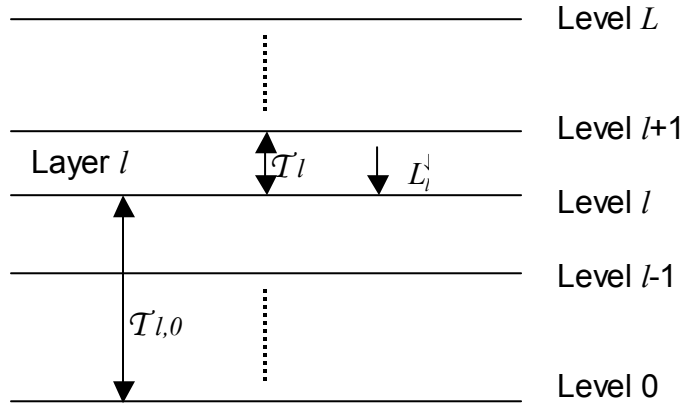
$$\frac{\partial L_0^\downarrow}{\partial \tau_l} = \left(B(\overline{T_l}) - L_{l+1}^\downarrow \right) \tau_{l+1,0} \quad (A.63)$$

A3.4.1.2 Upwelling OD partials $\frac{\partial L_L^\uparrow}{\partial \tau_l}$

We can write the upwelling radiance in terms of layer l as

$$L_L^\uparrow = \left[L_l^\uparrow \tau_l + B_{eff}(\overline{T}_l, T_{l+1}, \tau_l)(1 - \tau_l) \right] \tau_{l+1,L} + L_{l+1,L}^\uparrow \quad (\text{A.64})$$

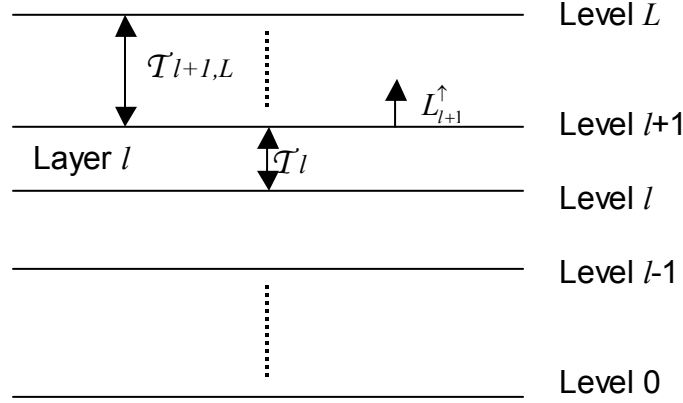
Figure A-8: Layer and level view for downwelling OD jacobian calculation



When $L_{l=0}^\uparrow$ is initialized to the surface term: $L_0^\uparrow = \varepsilon B(T_{sfc}) + \alpha L_0^\downarrow$ for nadir and to the “backside” or downwelling term: $L_0^\uparrow = L_0^\downarrow$ for limb, equation (A.64) becomes the total radiance at the satellite, L_{sat} , as given in equation (A.53). For the upwelling radiative transfer, we apply the linear-in-tau approximation described in section 3.3.1.4. Differentiating equation (A.64) gives

$$\frac{\partial L_L^\uparrow}{\partial \tau_l} = \left(B_{eff}(\overline{T}_l, T_{l+1}, \tau_l) - L_l^\uparrow \right) \tau_{l+1,L} + \frac{\partial B_{eff}}{\partial \tau_l} (1 - \tau_l) \tau_{l+1,L} \quad (\text{A.65})$$

Figure A-9: Layer and level view for upwelling OD jacobian calculation



Since $B_{eff}(\bar{T}_l, T_{l+1}, \tau_l) = B(\bar{T}_l) + \beta(\bar{T}_l, T_{l+1})F(\tau_l)$ where $\beta(\bar{T}_l, T_{l+1}) = B(T_{l+1}) - B(\bar{T}_l)$ and $F(\tau_l) = 1 - 2\left[\frac{1}{\tau_l} + \frac{T_l}{1 - T_l}\right]$; (with $F(\tau_l) = \frac{\tau_l}{6}$ for small values of τ_l), we have

$$\frac{\partial B_{eff}}{\partial \tau_l} = \beta \frac{\partial F}{\partial \tau_l} \quad (\text{A.66})$$

where $\frac{\partial F}{\partial \tau_l} = \frac{2}{\tau_l^2} - \frac{2T_l}{(1 - T_l)^2}$; (with $\frac{\partial F}{\partial \tau_l} = \frac{1}{6}$ for small τ_l) is pre-computed and tabulated in the same way as $F(\tau_l)$.

Combining the downwelling and upwelling terms, equation (A.59) becomes:

$$\frac{\partial L_{sat}}{\partial \tau_l} = (B_{eff}(\bar{T}_l, T_{l+1}, \tau_l) - L_l^{\uparrow})\mathcal{T}_{l,L} + \beta(\bar{T}_l, T_{l+1})\frac{\partial F}{\partial \tau_l}(1 - \tau_l)\mathcal{T}_{l+1,L} + \alpha(B(\bar{T}_l) - L_{l+1}^{\downarrow})\mathcal{T}_{l+1,0}\mathcal{T}_{0,L} \quad (\text{A.67})$$

Note that the term $-(\epsilon B(T_{sfc}) + \alpha L_0^{\downarrow})\mathcal{T}_{0,L}$ in equation (A.59) is accounted for since the upwelling radiance is initialized with $L_{l=0}^{\uparrow} = \epsilon B(T_{sfc}) + \alpha L_0^{\downarrow}$, for nadir, ($\epsilon=0$, $\alpha=1$ for limb).

A3.4.2 Partial of optical depth with respect to gas species VMR $\frac{\partial \tau_l}{\partial x_l}$

The layer optical depth is given by

$$\tau_l = \sum_m u_{l,m} \kappa_{l,m} = u_l \sum_m \kappa_{l,m} \bar{q}_{l,m} = u_l \kappa_l \quad (\text{A.68})$$

where $u_{l,m}$ is the integrated path amount in layer l for species m , $\kappa_{l,m}$ is the absorption coefficient and $\bar{q}_{l,m} = u_{l,m} / u_l$ is the layer average volume mixing ratio (VMR). For $m \neq 1$, i.e., all species except H_2O ,

$$\frac{\partial \tau_l}{\partial q_{l,m}} = u_l \kappa_{l,m} \quad \text{or} \quad \frac{\partial \tau_l}{\partial \ln q_{l,m}} = \bar{q}_{l,m} u_l \kappa_{l,m} = \tau_{l,m} \quad (\text{A.69})$$

We then have the simple result that the optical depth (OD) partial with respect to log VMR is simply the species optical depth.

A3.4.2.1 Partial of optical depth with respect to H_2O VMR $\frac{\partial \tau_l}{\partial q_{l,m=1}}$

For H_2O ($m=1$), we cannot neglect the dependence of H_2O VMR on self-broadening for

absorption coefficients $\left(\frac{\partial \kappa_{l,1}}{\partial q_{l,1}} \right)$ or the integrated path amount $\left(\frac{\partial u_l}{\partial q_{l,1}} \right)$ and we must separate the

absorption ($\kappa_{l,1}$) into both line (κ^{line}) and continuum (κ^{cont}) contributions. Including all these terms, we have

$$\frac{\partial \tau_l}{\partial \ln q_{l,1}} = \tau_{l,1} + \tau_{l,1}^{line} \frac{\partial \ln \kappa_{l,1}^{line}}{\partial \ln q_{l,1}} + \tau_{l,1}^{cont} \frac{\partial \ln \kappa_{l,1}^{cont}}{\partial \ln q_{l,1}} + \tau_l \frac{\partial \ln u_l}{\partial \ln q_{l,1}} \quad (\text{A.70})$$

Thus H_2O VMR jacobians have three additional terms that are computed, compared to the other gas species VMR jacobians. These terms are described in the following sub-sections.

A3.4.2.1.1 H_2O line self-broadening dependence $\tau_{l,1}^{line} \frac{\partial \ln \kappa_{l,1}^{line}}{\partial \ln q_{l,1}}$

We account for the self-broadening of H_2O absorption lines by tabulating two sets of absorption coefficients, κ^{wet} and κ^{dry} , for pressures > 100 mb. Line absorption for H_2O is then given by

$$\kappa_{l,1}^{line} = \kappa_l^{dry} + \left(\frac{\kappa_l^{wet} - \kappa_l^{dry}}{q_l^{wet} - q^{dry}} \right) (\bar{q}_{l,1} - q^{dry}) \quad (\text{A.71})$$

where q_l^{wet} is 90% of saturation vmr for the layer and q^{dry} is $1.0\text{e-}08$ (layer independent). We then have

$$\tau_{l,1}^{line} \frac{\partial \ln \kappa_{l,1}^{line}}{\partial \ln \bar{q}_{l,1}} = \bar{q}_{l,1} u_{l,1} \left(\frac{\kappa_l^{wet} - \kappa_l^{dry}}{\bar{q}_l^{wet} - \bar{q}_l^{dry}} \right) \quad (A.72)$$

A3.4.2.1.2 H₂O continuum dependence $\tau_{l,1}^{cont} \frac{\partial \ln \kappa_{l,1}^{cont}}{\partial \ln \bar{q}_{l,1}}$

From equation 3.27, the absorption coefficient for water vapor continuum is given by:

$$\kappa_{l,1}^{cont} = \nu \tanh \left(\frac{h\nu}{2k_B \bar{T}_l} \right) \left[\frac{\bar{P}_l \bar{T}_o}{\bar{P}_o \bar{T}_l} \right] \left(\bar{q}_{l,1} C_s (\bar{T}_l) + (1 - \bar{q}_{l,1}) C_f \right) \quad (A.73)$$

where C_s and C_f are the self and foreign broadened coefficients, respectively. We then have:

$$\tau_{l,1}^{cont} \frac{\partial \ln \kappa_{l,1}^{cont}}{\partial \ln \bar{q}_{l,1}} = u_{l,1} \kappa_{l,1}^{cont} \left(\frac{\bar{q}_{l,1} (C_s - C_f)}{\bar{q}_{l,1} C_s + (1 - \bar{q}_{l,1}) C_f} \right) \quad (A.74)$$

A3.4.2.1.3 Layer integrated path amount dependence on H₂O VMR $\tau_l \frac{\partial \ln u_l}{\partial \ln \bar{q}_{l,1}}$

Because water vapor at altitudes below 100mb is abundant enough to affect the integrated path amount through those layers, we account for this dependence in the H₂O VMR jacobians. For nadir and most limb layers (all but the tangent and next to tangent layers), we can assume a straight path through the layer, *i.e.*, refraction can be neglected over the layer height. In these cases, we can write

$$g(M_{dry} u_l + M_{H_2O} \bar{q}_{l,1} u_l) = c \Delta p = \text{constant} \quad (A.75)$$

since we have a fixed pressure grid with Δp and we can assume gravitational acceleration, g , is constant over the layer. M_{dry} and M_{H_2O} are the molecular weights of dry air and water respectively. The constant c is the geometric correction for any straight path with respect to vertical ($c=1$ for a vertical path). Differentiating this expression gives

$$\frac{\partial \ln u_l}{\partial \ln \bar{q}_{l,1}} = \frac{-1}{1 + \left(\frac{M_{dry}}{\bar{q}_{l,1} M_{H_2O}} \right)} \quad (A.76)$$

where $\frac{M_{dry}}{M_{H_2O}} = \frac{28.96}{18} = 1.609$. In general, the contribution from this term is small

(<1%) compared to the other corrections for H₂O VMR jacobians.

The values of equation (A.76) have been compared to finite difference calculations with the ray-tracing code. For nadir and non-tangent layers for limb, the differences between this expression and the finite difference calculations are at most 3%. For limb tangent layers, the differences are around 30%. However, the effects of this correction are further reduced since it is subsequently

multiplied by total transmission, which will be small in the limb case for layers near the surface where this correction is largest, due to water vapor continuum. Since we do not detect significant differences in the overall comparison of analytic to finite difference for limb H₂O VMR jacobians due to the presence or absence of this term, we are not planning to modify the calculation in the limb tangent layers at this time.

A3.4.3 Partial with respect to layer Planck (or effective Planck) function

$$\frac{\partial L_{sat}}{\partial B_l}$$

Differentiating (A.53), we obtain

$$\frac{\partial L_{sat}}{\partial B_l} = \frac{\partial L_l^\uparrow}{\partial B_l} + \alpha \frac{\partial L_0^\downarrow}{\partial B_l} \tau_{0,L} \quad (\text{A.77})$$

Downwelling term

Following equation (A.62), $L_0^\downarrow = [L_{l+1}^\downarrow \tau_l + B_l (1 - \tau_l)] \tau_{l,0} + L_{l,0}^\downarrow$ and

$$\frac{\partial L_0^\downarrow}{\partial B_l} = (1 - \tau_l) \tau_{l,0} \quad (\text{A.78})$$

Upwelling term

From equation (A.64), $L_L^\uparrow = [L_l^\uparrow \tau_l + B_l^{eff} (1 - \tau_l)] \tau_{l+1,L} + L_{l+1,L}^\uparrow$ and

$$\frac{\partial L_L^\uparrow}{\partial B_l^{eff}} = (1 - \tau_l) \tau_{l+1,L} \quad (\text{A.79})$$

where B_l^{eff} is the layer effective Planck function for upwelling radiance calculations, assuming the linear-in-tau approximation, as discussed in section 3.3.1.4.

A3.4.4 Partial of layer Planck (or effective Planck) function with respect to temperature $\frac{\partial B_l}{\partial T_l}$

The Planck function (in W/m²/sr/cm⁻¹) is given by $B_l = \frac{2hc^2\nu^3}{\exp\left(\frac{h\nu}{k_B \bar{T}_l}\right) - 1}$ with partial:

$$\frac{\partial B_l}{\partial \bar{T}_l} = \frac{B_l^2 \exp\left(\frac{h\nu}{k_B \bar{T}_l}\right)}{2c\nu^2 k_B \bar{T}_l^2} \quad (\text{A.80})$$

For the effective Planck function $B_l^{eff} = B_l + \beta(\bar{T}_l, T_{l+1}) F(\tau_l)$ with $\beta = B(T_{l+1}) - B(\bar{T})$, (see equation (A.66) for $F(\tau_l)$), we have

$$\frac{\partial B_l^{eff}}{\partial \overline{T}_l} = \frac{\partial B_l}{\partial \overline{T}_l} + F(\tau_l) \left[\frac{\partial B}{\partial T_{l+1}} \frac{\partial T_{l+1}}{\partial \overline{T}_l} - \frac{\partial B_l}{\partial \overline{T}_l} \right] \quad (\text{A.81})$$

where $\frac{\partial T_{l+1}}{\partial \overline{T}_l}$ is the inverse layer-to-level partial for temperature given in section A3.4.6, with $T_{l+1} = T_U$, i.e., the temperature at the upper level of layer l .

A3.4.5 Partial of optical depth with respect to temperature $\frac{\partial \tau_l}{\partial \overline{T}_l}$

Accounting directly for both line and continuum absorption, equation (A.68) becomes

$$\tau_l = \sum_m u_{l,m} (\kappa_{l,m}^{line} + \kappa_{l,m}^{cont}) \quad (\text{A.82})$$

with

$$\frac{\partial \tau_l}{\partial \overline{T}_l} = \sum_m u_{l,m} \left(\frac{\partial \kappa_{l,m}^{line}}{\partial \overline{T}_l} + \frac{\partial \kappa_{l,m}^{cont}}{\partial \overline{T}_l} \right) + \kappa_{l,m} \frac{\partial u_{l,m}}{\partial \overline{T}_l} \quad (\text{A.83})$$

Note that we are neglecting the dependence of the integrated path amounts in layers k where $k > l$ on \overline{T}_l , which is small, but may need further study.

A3.4.5.1 Partial of line absorption with respect to temperature $\frac{\partial \kappa_{l,m}^{line}}{\partial \overline{T}_l}$

Line absorption coefficients are determined by a 3-point Lagrange interpolation in temperature, with $\kappa_{l,m}^{line} = \sum_{i=0}^2 c_i(\overline{T}_l) \kappa_{i,(l,m)}$ where $\kappa_{i,(l,m)}$ is the absorption coefficient tabulated at temperature T_i , in layer l for species m . Lagrange interpolation gives

$$c_i(x) = \frac{(x - x_0) \dots (x - x_{i-1})(x - x_{i+1}) \dots (x - x_n)}{(x_i - x_0) \dots (x_i - x_{i-1})(x_i - x_{i+1}) \dots (x_i - x_n)} \text{ and for 3-point interpolation, we have}$$

$$c_0(\overline{T}_l) = \left[(T_1 - T_2) \overline{T}_l^2 + (T_2^2 - T_1^2) \overline{T}_l + (T_1^2 T_2 - T_1 T_2^2) \right] / D$$

$$c_1(\overline{T}_l) = \left[(T_2 - T_0) \overline{T}_l^2 + (T_0^2 - T_2^2) \overline{T}_l + (T_2^2 T_0 - T_2 T_0^2) \right] / D$$

$$c_2(\overline{T}_l) = \left[(T_0 - T_1) \overline{T}_l^2 + (T_1^2 - T_0^2) \overline{T}_l + (T_0^2 T_1 - T_0 T_1^2) \right] / D$$

where D is the common denominator: $D = T_0^2(T_1 - T_2) + T_1^2(T_2 - T_0) + T_2^2(T_0 - T_1)$

The temperature partials are then

$$\frac{\partial \kappa_{l,m}^{line}}{\partial T_l} = \sum_{i=0}^2 \frac{\partial c_i}{\partial T_l} \kappa_{i,(l,m)} \quad (\text{A.84})$$

where

$$\begin{aligned} \frac{\partial c_0}{\partial T_l} &= [2(T_1 - T_2)\overline{T_l} + (T_2^2 - T_1^2)]/D \\ \frac{\partial c_1}{\partial T_l} &= [2(T_2 - T_0)\overline{T_l} + (T_0^2 - T_2^2)]/D \\ \frac{\partial c_2}{\partial T_l} &= [2(T_0 - T_1)\overline{T_l} + (T_1^2 - T_0^2)]/D \end{aligned} \quad (\text{A.85})$$

A3.4.5.2 Partial of continuum absorption with respect to temperature $\frac{\partial \kappa_{l,m}^{cont}}{\partial T_l}$

For species m , ($m=\text{H}_2\text{O}$, CO_2 , N_2 , O_2), the CKD v3.0 continuum model (see section 3.3.8.4 and references therein) has tabulated coefficients for use in the following expression for continuum absorption:

$$\kappa_{l,m}^{cont}(\nu, \overline{T_l}, \overline{P_l}) = R(\nu, \overline{T_l}) C_m(\nu, \overline{T_l}, \overline{P_l}) \quad \text{where} \quad R(\nu, \overline{T_l}) = \nu \tanh\left(\frac{h\nu}{2k_B \overline{T_l}}\right) \quad (\text{A.86})$$

For any m ,

$$\frac{\partial \kappa_{l,m}^{cont}}{\partial T_l} = \frac{\partial R}{\partial T_l} C_m + R \frac{\partial C_m}{\partial T_l} \quad (\text{A.87})$$

and

$$\frac{\partial R}{\partial T_l} = \frac{hc}{2k_B \overline{T_l}^2} (R^2 - \nu^2) \quad (\text{A.88})$$

A3.4.5.2.1 Temperature partials for water vapor continuum coefficient $\frac{\partial C_{\text{H}_2\text{O}}}{\partial T_l}$

For H_2O , $C_{\text{H}_2\text{O}} = (C_S(\overline{T_l})\overline{q_l} + C_F(1 - \overline{q_l})) \frac{\overline{P_l}}{P_o} \frac{T_o}{\overline{T_l}}$ where $P_o = 1013$ hPa, $T_o = 296$ K and

$$C_S(\overline{T_l}) = C_{S-296} \left(\frac{C_{S-260}}{C_{S-296}} \right)^{T_{fac}}; T_{fac} = \frac{\overline{T_l} - T_o}{260 - T_o} \quad \text{with temperature partial}$$

$$\frac{\partial C_{H_2O}}{\partial \overline{T}_l} = -\frac{C_{H_2O}}{\overline{T}_l} + \overline{q}_l \frac{\overline{P}_l}{P_o} \frac{T_o}{\overline{T}_l} \left(\frac{C_s \ln C_s}{260 - T_o} \right) \quad (A.89)$$

A3.4.5.2.2 Temperature partials for carbon dioxide continuum coefficient $\frac{\partial C_{CO_2}}{\partial \overline{T}_l}$

For the CO₂ continuum, $C_{CO_2} = C_F \frac{\overline{P}_l}{P_o} \frac{T_o}{\overline{T}_l}$ with temperature partial

$$\frac{\partial C_{CO_2}}{\partial \overline{T}_l} = -\frac{C_{CO_2}}{\overline{T}_l} \quad (A.90)$$

A3.4.5.2.3 Temperature partials for nitrogen continuum coefficient $\frac{\partial C_{N_2}}{\partial \overline{T}_l}$

For the N₂ continuum, $C_{N_2} = C_F \frac{\overline{P}_l}{P_o} \frac{T_o}{\overline{T}_l}$ with temperature partial \

$$\frac{\partial C_{N_2}}{\partial \overline{T}_l} = -\frac{C_{N_2}}{\overline{T}_l} \quad (A.91)$$

A3.4.5.2.4 Temperature partials for oxygen continuum coefficient $\frac{\partial C_{O_2}}{\partial \overline{T}_l}$

For the O₂ continuum, $C_{O_2} = C_F \frac{\overline{P}_l}{P_o} \exp \left(C_1 (\overline{T}_l - 220) + C_2 (\overline{T}_l - 220)^2 \right)$ with temperature partial

$$\frac{\partial C_{O_2}}{\partial \overline{T}_l} = C_{O_2} \left[C_1 + 2C_2 (\overline{T}_l - 220) \right] \quad (A.92)$$

A3.4.5.3 Partial of layer integrated path amounts with respect to temperature $\frac{\partial u_{l,m}}{\partial \overline{T}_l}$

This term is only important in the tangent and next-to-tangent layers in the limb mode where neglecting the term results in about a 10% difference between analytic and finite difference jacobians for the TES detectors and about 25% difference for individual rays. It has a negligible

contribution to nadir temperature jacobians. An analytic expression for $\frac{\partial u_{l,m}}{\partial \overline{T}_l}$ where $u_{l,m}$ is

calculated in the ray-tracing module would be quite difficult given the dependence of density, altitude (*via* the hydrostatic equation) and index of refraction on temperature. We therefore

propose a finite difference calculation using the ray-tracing algorithm only. Since this partial does not depend on frequency, this should not be too expensive computationally. Also, we will not need to compute this term for all layers in each limb ray, only those closest to and including the tangent layer. The necessary number of layers will be determined by prototyping the ray-tracing finite difference calculation for this term.

A3.4.6 Layer-to-Level Jacobians

The frequency independent partials that relate layer average quantities to the parameters specified on and retrieved on levels must be computed in the same manner as the layer average quantities in the ray-tracing algorithm. Simpler approximations to this mapping, such as linear-in-log pressure interpolation were found to be unacceptably inaccurate.

These jacobians have rather lengthy derivations, which are given in TES Algorithm & Science DFM #217 by H. Worden & S. Sund, July, 2001. Only the results of the derivations will be repeated here. Following equation (A.54), for both limb and nadir cases, we are interested in the following partials:

$$\frac{\partial \ln \bar{q}_{l,m}}{\partial \ln \bar{q}_{L,m}} \text{ and } \frac{\partial \ln \bar{q}_{l,m}}{\partial \ln \bar{q}_{U,m}}; \quad \frac{\partial \bar{T}_l}{\partial T_L} \text{ and } \frac{\partial \bar{T}_l}{\partial T_U}$$

where levels L (lower) and U (upper) bound layer l . For limb cases, path-weighted layer average quantities are computed using a sum over sub-layers, the number and size of which are determined dynamically, with the tangent layer having the most sub-layers. For nadir cases, given our relatively fine forward model pressure grid, it is sufficient to use single layers (*i.e.*, no sub-layers) to compute the path-weighted layer average quantities.

A3.4.6.1 Limb layer-to-level VMR Jacobians

The layer vmr, $\bar{q}_{l,m}$, for species m is the integrated species amount divided by the total path amount u_l :

$$\bar{q}_{l,m} = \frac{H_{\rho,m}}{u_l} \sum_{i=L}^{U-1} \frac{\Delta s_i}{\Delta r_i} (\rho_{i,m} - \rho_{i+1,m}) \quad (\text{A.93})$$

where $H_{\rho,m}$ is the species density scale height: $H_{\rho,m} = -\frac{r_U - r_L}{\ln\left(\alpha \frac{q_{U,m}}{q_{L,m}}\right)}$ with $\alpha = \frac{\rho_U}{\rho_L} = \frac{P_U/T_U}{P_L/T_L}$ and

spherical layer upper and lower radii r_U and r_L . $\frac{\Delta s_i}{\Delta r_i}$ is the ratio of line-of-sight distance through sub-layer i over sub-layer height, and the sub-layer species density is given by:

$$\rho_{i,m} = \rho_{L,m} \exp\left(-\frac{r_i - r_L}{H_{\rho,m}}\right).$$

The layer-to-level VMR jacobians are:

$$\frac{\partial \ln \bar{q}_{l,m}}{\partial \ln q_{L,m}} = \frac{H_{\rho,m}}{q_{l,m} u_l} \left[\sum_{i=L}^{U-1} \frac{\Delta s_i}{\Delta r_i} \left\{ \rho_{i,m} \left(\frac{r_U - r_i}{r_U - r_L} \right) - \rho_{i+1,m} \left(\frac{r_U - r_{i+1}}{r_U - r_L} \right) \right\} \right] + \frac{1}{\ln \left(\alpha \frac{q_{U,m}}{q_{L,m}} \right)} \quad (\text{A.94})$$

$$\frac{\partial \ln \bar{q}_{l,m}}{\partial \ln q_{U,m}} = \frac{H_{\rho,m}}{q_{l,m} u_l} \left[\sum_{i=L}^{U-1} \frac{\Delta s_i}{\Delta r_i} \left\{ \rho_{i,m} \left(\frac{r_i - r_L}{r_U - r_L} \right) - \rho_{i+1,m} \left(\frac{r_{i+1} - r_L}{r_U - r_L} \right) \right\} \right] - \frac{1}{\ln \left(\alpha \frac{q_{U,m}}{q_{L,m}} \right)} \quad (\text{A.95})$$

It is easily verified that equation (A.94) and (A.95) add to 1, which they must in order to have

$$\bar{q}_{l,m} = \frac{\partial \bar{q}_{l,m}}{\partial q_L} q_L + \frac{\partial \bar{q}_{l,m}}{\partial q_U} q_U = \frac{\bar{q}_{l,m}}{q_L} \left(\frac{\partial \ln \bar{q}_{l,m}}{\partial \ln q_L} \right) q_L + \frac{\bar{q}_{l,m}}{q_U} \left(\frac{\partial \ln \bar{q}_{l,m}}{\partial \ln q_U} \right) q_U$$

A3.4.6.2 Limb layer-to-level Temperature Jacobians

The layer temperature, \bar{T}_l , is given by:

$$\bar{T}_l = \frac{H_\rho}{u_l} \sum_{i=L}^{U-1} \frac{\Delta s_i}{\Delta r_i} (\rho_i T_i - \rho_{i+1} T_{i+1}) - T_H \quad (\text{A.96})$$

where $T_H = H_\rho \left(\frac{T_U - T_L}{r_U - r_L} \right) = - \frac{(T_U - T_L)}{\ln(\rho_U/\rho_L)}$,

density scale height $H_\rho = - \frac{r_U - r_L}{\ln(\rho_U/\rho_L)}$, sub-layer density is given by $\rho_i = \rho_L \exp\left(-\frac{r_i - r_L}{H_\rho}\right)$ and sub-

layer temperature is given by linear in log pressure interpolation: $T_i = a + b \ln P_i$ with

$$a = T_L - \frac{\ln P_L}{\ln(P_U/P_L)} (T_U - T_L) \text{ and } b = \frac{T_U - T_L}{\ln(P_U/P_L)}.$$

The layer-to-level temperature jacobians are:

$$\begin{aligned} \frac{\partial \bar{T}_l}{\partial T_L} &= \frac{H_\rho}{u_l T_L} \sum_{i=L}^{U-1} \frac{\Delta s_i}{\Delta r_i} \left\{ \rho_i \left(\frac{r_U - r_i}{r_U - r_L} \right) (\bar{T}_l - T_H + T_L - T_i) - \rho_{i+1} \left(\frac{r_U - r_{i+1}}{r_U - r_L} \right) (\bar{T}_l - T_H + T_L - T_{i+1}) \right\} \\ &\quad - \frac{H_\rho}{r_U - r_L} \left(1 - \frac{T_H}{T_L} \right) \end{aligned} \quad (\text{A.97})$$

$$\begin{aligned} \frac{\partial \bar{T}_l}{\partial T_U} &= \frac{H_\rho}{u_l T_U} \sum_{i=L}^{U-1} \frac{\Delta s_i}{\Delta r_i} \left\{ \rho_i \left(\frac{r_U - r_i}{r_U - r_L} \right) (\bar{T}_l - T_H + T_U - T_i) - \rho_{i+1} \left(\frac{r_U - r_{i+1}}{r_U - r_L} \right) (\bar{T}_l - T_H + T_U - T_{i+1}) \right\} \\ &\quad + \frac{H_\rho}{r_U - r_L} \left(1 - \frac{T_H}{T_U} \right) \end{aligned} \quad (\text{A.98})$$

A3.4.6.3 Nadir layer-to-level VMR Jacobians

When sub-layers are not applied, the layer average quantities reduce to simpler expressions. We then have layer-to-level VMR jacobians:

$$\frac{\partial \ln \bar{q}_{l,m}}{\partial \ln q_{L,m}} = \frac{q_{L,m}}{q_{L,m} - \alpha q_{U,m}} + \frac{1}{\ln\left(\alpha \frac{q_{U,m}}{q_{L,m}}\right)} \quad (\text{A.99})$$

$$\frac{\partial \ln \bar{q}_{l,m}}{\partial \ln q_{U,m}} = \frac{-\alpha q_{U,m}}{q_{L,m} - \alpha q_{U,m}} - \frac{1}{\ln\left(\alpha \frac{q_{U,m}}{q_{L,m}}\right)} \quad (\text{A.100})$$

A3.4.6.4 Nadir layer-to-level Temperature Jacobians

Likewise, the layer average temperature expression becomes simpler and the layer-to-level temperature jacobians are:

$$\frac{\partial \bar{T}_l}{\partial T_L} = \frac{\bar{T}_l - T_H}{T_L} \left(\frac{\rho_L}{\rho_L - \rho_U} \right) + \frac{1}{\ln\left(\rho_U/\rho_L\right)} \left(1 - \frac{T_H}{T_L} \right) \quad (\text{A.101})$$

$$\frac{\partial \bar{T}_l}{\partial T_U} = \frac{\bar{T}_l - T_H}{T_U} \left(\frac{-\rho_L}{\rho_L - \rho_U} \right) - \frac{1}{\ln\left(\rho_U/\rho_L\right)} \left(1 - \frac{T_H}{T_U} \right) \quad (\text{A.102})$$

where $T_H = -\frac{(T_U - T_L)}{\ln\left(\rho_U/\rho_L\right)}$.

A3.4.7 Pointing Jacobians

The field of view integration for the radiance measured with detector d , from section 3.3.6 is given by

$$L_{sat}(\theta_d) = \sum_{j=0}^{N_{FOV}} L(\theta_j) \mathbf{R}_{FOV}(\theta_j - \theta_d) \Delta\theta_j \quad (\text{A.103})$$

Writing this as an integral,

$$L_{sat}(\theta_d) = \int_{\theta_{\min}}^{\theta_{\max}} L(\theta) \mathbf{R}_{FOV}(\theta - \theta_d) d\theta \quad (\text{A.104})$$

Since $\frac{\partial \mathbf{R}_{FOV}}{\partial \theta_d} = -\frac{\partial \mathbf{R}_{FOV}}{\partial \theta}$, we have

$$\frac{\partial L_{sat}}{\partial \theta_d} = \int_{\theta_{min}}^{\theta_{max}} L(\theta) \left(-\frac{\partial R_{FOV}}{\partial \theta} \right) d\theta \quad (A.105)$$

Integration by parts gives

$$\frac{\partial L_{sat}}{\partial \theta_d} = -L(\theta) R_{FOV}(\theta - \theta_d) \Big|_{\theta_{min}}^{\theta_{max}} + \int_{\theta_{min}}^{\theta_{max}} \left(\frac{\partial L}{\partial \theta} \right) R_{FOV}(\theta - \theta_d) d\theta \quad (A.106)$$

Assuming we have chosen θ_{min} and θ_{max} to be angles where the detector response is negligible, the first term in equation (A.106) is zero. This leaves the second term, which we write as a sum:

$$\frac{\partial L_{sat}}{\partial \theta_d} = \sum_{j=0}^{N_{FOV}} \left(\frac{\partial L}{\partial \theta_j} \right) R_{FOV}(\theta_j - \theta_d) \Delta \theta_j \quad (A.107)$$

This now has the same form as equation (A.103) with $L(\theta_j)$ replaced by $\frac{\partial L}{\partial \theta_j}$. The $\frac{\partial L_{sat}}{\partial \theta_d}$ partials are then computed in the same way we compute detector radiances, with the switch to ray indices as described in section 3.3.6.

For 4-point Lagrange interpolation, $L(\theta_j) = \sum_{m=-1}^2 a_{j,m} L(\theta_{k+m})$ and we have

$$\frac{\partial L}{\partial \theta_j} = \sum_{m=-1}^2 \frac{\partial a_{j,m}}{\partial \theta_j} L(\theta_{k+m}) \quad (A.108)$$

Since the interpolation coefficients are defined with respect to the variable p , with $p = \frac{\theta_j - \theta_k}{\theta_{k+1} - \theta_k}$,

we have

$$\frac{\partial a_{j,m}}{\partial \theta_j} = \frac{\partial a_{j,m}}{\partial p} \frac{\partial p}{\partial \theta_j} = \frac{\partial a_{j,m}}{\partial p} \left(\frac{1}{\theta_{k+1} - \theta_k} \right) \quad (A.109)$$

where

$$\begin{aligned}
 \frac{\partial a_{j,-1}}{\partial p} &= (-1 + 4p - 3p^2) / (1 + c_1) \\
 \frac{\partial a_{j,0}}{\partial p} &= 6p(p-1) + p(2-3p) / (1 + c_2) \\
 \frac{\partial a_{j,1}}{\partial p} &= 6p(1-p) + (1-4p+3p^2) / (1 + c_1) \\
 \frac{\partial a_{j,2}}{\partial p} &= (3p^2 - 2p) / (1 + c_2)
 \end{aligned}
 \tag{A.110}$$

with $c_1 = (\theta_k - \theta_{k-1}) / (\theta_{k+1} - \theta_k)$ and $c_2 = (\theta_{k+2} - \theta_{k+1}) / (\theta_{k+1} - \theta_k)$.

As noted above, these partials of the interpolation coefficients are then propagated along with the interpolation coefficients to obtain both detector radiances and pointing jacobians.

A3.4.8 Jacobian Validation

NOTE: THIS SECTION IS UNDER CONSTRUCTION

We validate our analytic jacobians by comparing to jacobians computed by the finite difference (FD) method described in section 3.4.1.

A3.4.8.1 Nadir Jacobian Validation

Table A-3: Nadir jacobian comparisons: Finite Difference (FD) to Analytic

Retrieved Parameter	Frequency Range (cm ⁻¹)	Max FD value	Max FD-Analytic	RMS FD-Analytic
Temperature at 619 mb	760-785	2.37e-08	1.1e-10	2.0e-11
H ₂ O at 750 mb	1202-1214	1.80e-07	4.8e-09	8.7e-10

Figure A-10:

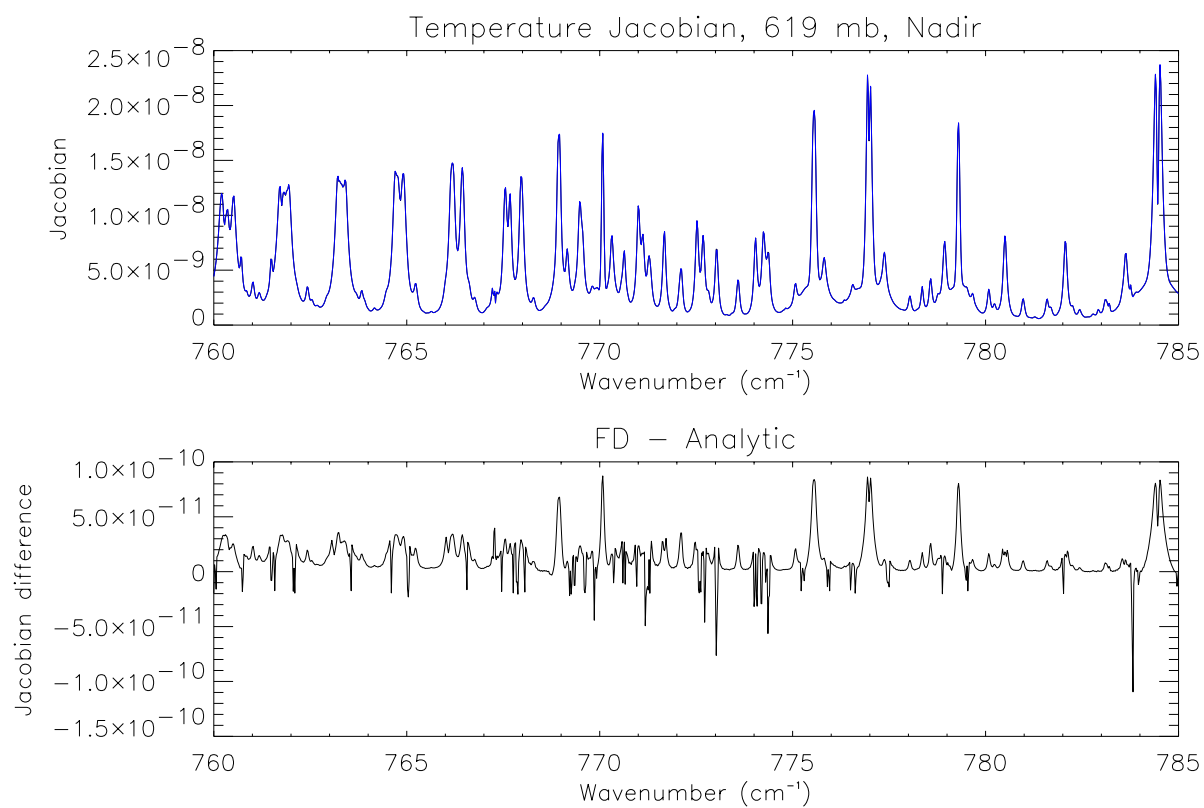
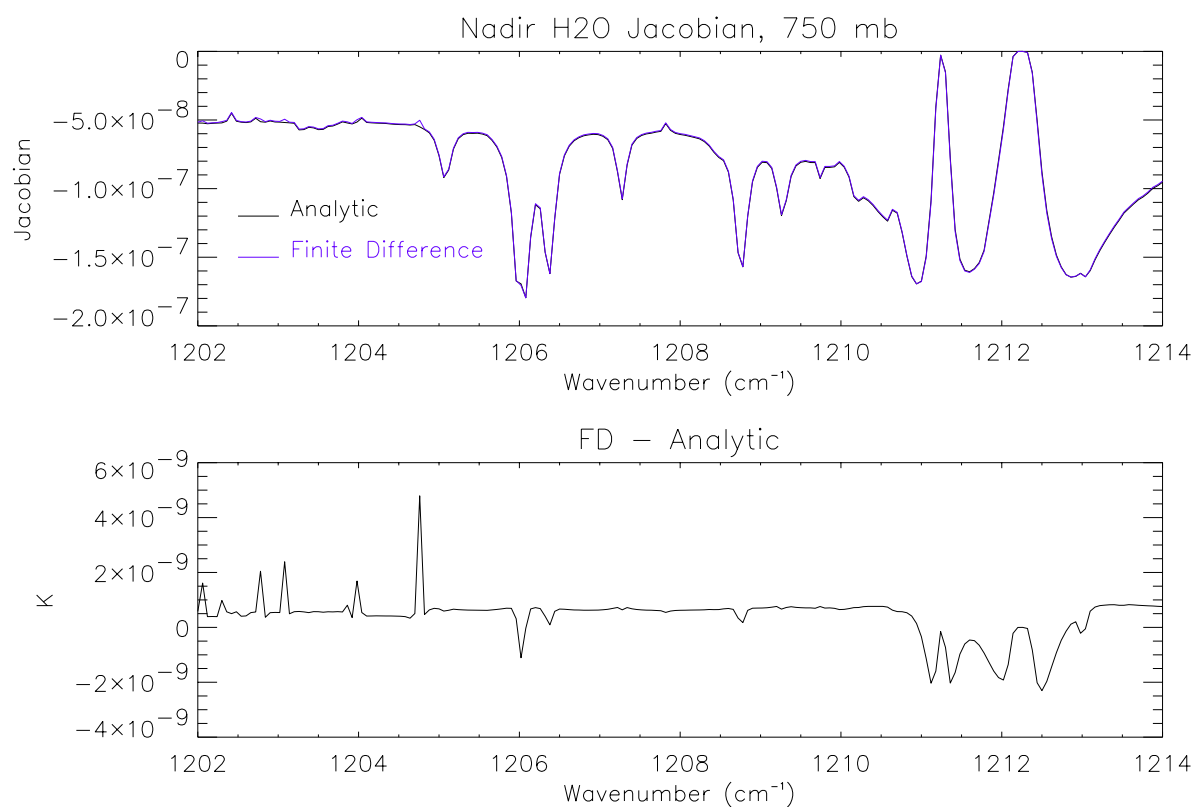


Figure A-11:

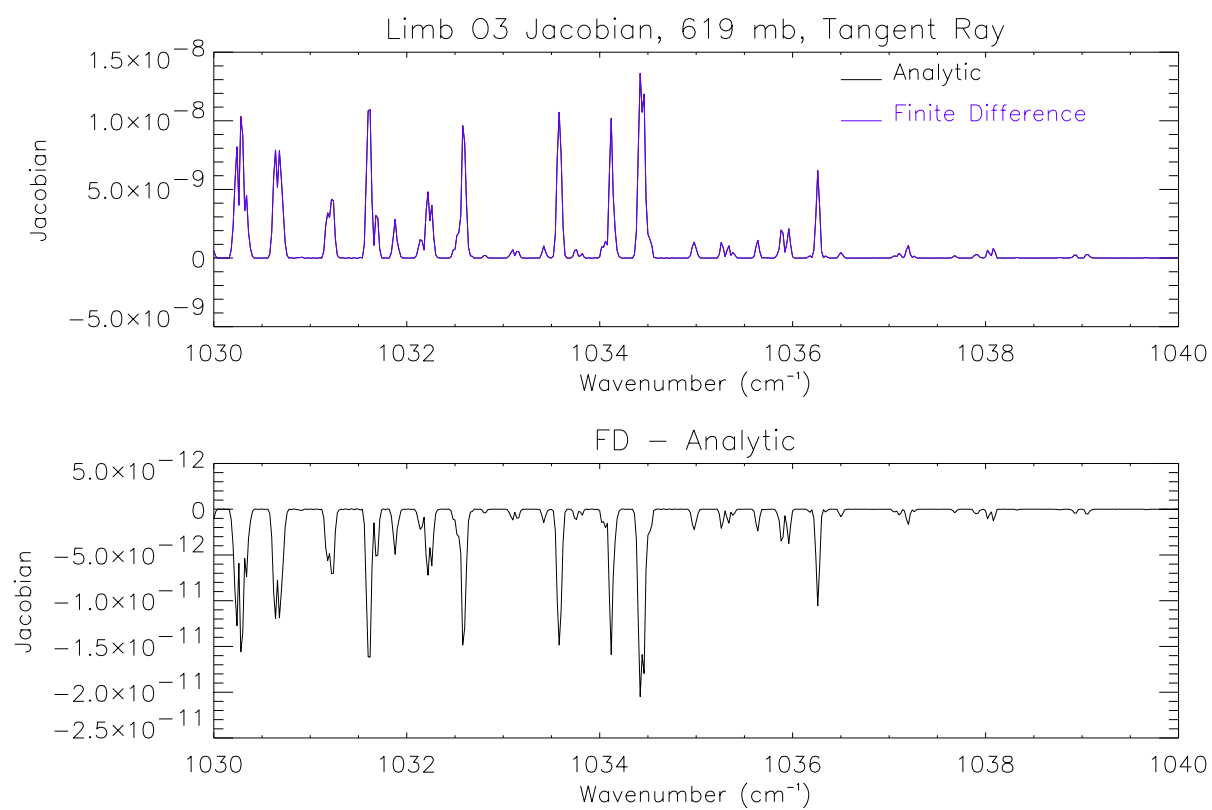


A3.4.8.2 Limb Jacobian Validation

TableA- 4: Limb jacobian comparisons: Finite Difference (FD) to Analytic

Retrieved Parameter	Frequency Range (cm^{-1})	Limb Ray Tangent Pressure	Max FD value	Max FD-Analytic	RMS FD-Analytic
O ₃ at 619 mb	1030-1040	1000 mb	2.71e-08	3.6e-11	6.4e-12
		909 mb	2.47e-08	3.0e-11	5.6e-12
		825 mb	2.20e-08	2.1e-11	4.6e-12
		750 mb	1.78e-08	1.7e-11	3.8e-12
		681 mb	6.79e-09	6.0e-12	1.2e-12
		619 mb	1.34e-08	2.0e-11	3.3e-12
H ₂ O at 750 mb	1204-1214	1000 mb	2.06e-07	1.2e-09	5.8e-10
		909 mb	2.02e-07	3.3e-10	1.3e-10
		825 mb	1.08e-07	1.7e-10	1.0e-10
		750 mb	4.61e-07	6.4e-10	2.2e-10

Figure A-12:



A3.5.1 Retrieval Strategy

This appendix gives descriptions of the retrieval strategy suppliers listed in section 3.5.1.2 and 3.5.1.3.

Target level suppliers:

Strategy Table.

Strategy table parameters are read and organized so to make the strategy table information is easily accessible by the other suppliers.

Surface pressure.

If the level 1b cloud flag indicates low intrapixel variability, the scene may be either cloud free or cloud filled. To distinguish between cloud free or cloud filled, the difference between the surface temperature and the brightness temperature in a particular part of the spectrum will be calculated, which may require a RT calculation to account for transmission through the water vapor continuum (See also the pixel categorization section, 3.5.5 for nadir, or 3.5.6 for limb). (1) If this difference is small, the scene is considered clear; the surface pressure is calculated at the surface altitude (an input) using the hydrostatic equation and the sea surface pressure, lowest atmospheric temperature, and lowest atmospheric water values. (2) If this difference is large and the intrapixel variability of BT11 is low, this will be identified as a retrievable cloud filled scene. BT11 will then be compared against the temperature profile to determine the pressure level of the new surface, which will have the emissivity of a cloud. Note: cloud height top may be determined by an adaptation of CO₂ slicing rather than a simple comparison of BT and the temperature profile.

Forward model pressure.

Once the surface pressure has been determined, the FMPressure vector is created starting from the standard pressure grid: (1) Cut off the levels below the surface pressure on the standard pressure grid. (2) Add a level at the surface pressure. (3) Possibly remove the pressures adjacent to the surface pressure if they are too close (the current cutoff is .1%).

Target level full state vector (initial guess).

Gather information for the initial state vector described in section 3.2.2. For each species, use one or multiple sources (specified in the strategy table) to create a single profile. For an atmospheric species: (1) interpolate from the pressure levels of the sources to FMPressures. (2) If the control parameter specifies it, project the initial guess to within the span of the retrieval vector using the maps created in the map supplier. (3) Also, have the capability of creating hybrid profiles using meteorological data and other specified parameters, for example interpolate from a profile to the meteorologically specified surface value.

True full state vector.

This is only used for data simulation and error analysis of simulated data. The true full state needs all of the functionality of the Sequence Level Full State Vector and can use the same class

as the Sequence Level Full State Vector, but with different sources provided by the strategy table.

Target level emissivity.

Create a vector of emissivity vs. frequency. If there are no clouds, access the land cover database to determine the land cover types and amount of each type in the target scene footprint, and access the emissivity database to get the emissivity of the footprint based on the land cover types and amount of each type in the footprint. If there are clouds, get the cloud emissivity from a cloud database.

Target level map.

Create maps from retrieval parameters to forward model levels and vice versa. (see section 3.5.2.1). Calculate (from retrieval levels) or read in a map and inverse map for each atmospheric species in all steps. If maps are read in, they will be on the standard pressure grid and must be modified to the FMPressures grid. Although conceptually this is a step-level supplier, the maps are needed for projecting the initial guess before the first step. See section 3.5.2.1 for a more detailed description of mapping)

Simulated spectrum.

Simulates radiance data using the true state. This is only used for data simulation. The output data is formatted exactly like real data.

Measured spectrum.

Average spectra information (for scans and pixels, nadir only) and RMS the noise over pixels and scan, depending on the view mode (nadir vs. limb) and control information (bad pixel or bad scan information).

Target level Microwindows definitions.

Access a database of microwindow ranges to select the correct list of microwindows for each step or combined microwindows for all steps. The database of microwindows are arranged by retrieval species and view mode, and may be arranged by location or season. For each microwindow, it must also get the list of forward model species, filter, and detector mask (occupation matrix). Although conceptually this is a step-level supplier, all the microwindows are needed for simulating data, if data is simulated on an as-needed basis.

Step level suppliers:

Step level map.

Get maps for this step for all atmospheric species from the Target Level Map Supplier.

Step level Microwindows definitions.

Get relevant information from Target Level Microwindows Definitions Supplier for this step.

A priori x_a .

This supplier has the same requirements as the Target level full state supplier, with different source instances. It must also map to the retrieval parameters in the case of an atmospheric species. It must get have access to the results of the emissivity supplier to get the retrieval parameters for emissivity.

A priori constraint.

Create the full constraint matrix (which is square with dimension = # retrieval parameters) as described in section 3.5.3.

A priori climatology covariance.

Create the full covariance matrix (which is square with dimension = # retrieval parameters) to be used in error analysis as described in section 3.5.9.

Microwindows radiances.

Pick out the radiances in the given microwindows. Use the noise vector to deweight particular frequencies with the occupation matrix. Provides the radiances and noise for the retrieval microwindows in this step.

Emissivity a priori.

Select the emissivity retrieval frequencies based on the microwindow information, results of the target level emissivity supplier, and control parameters. Create the constraint matrix and true covariance for emissivity similarly to the other constraint matrices but with perhaps different control parameters. Create the a priori vector of emissivity by selecting the initial guess values at the retrieval frequencies.

Step level full state vector.

Get the information from the updated target level full state vector needed for the step level full state vector.

Retrieval levels.

Access a database of retrieval levels to get the retrieval levels for the specified view mode, location, species, and maptype. The retrieval levels in the database are associated with the pressures in StandardPressureLevels and must be adjusted to the FMPressures by the following steps:

- (1) Remove levels outside of FMPressures.
- (2) Reindex levels so that the level corresponding to the lowest FMPressures is level 1.
- (3) Add or move levels so that there is always a retrieval level associated with the lowest and highest FMPressures. There is a threshold for when to add a new level versus move an existing level.

REFERENCES

A3.3.1.1: Ray Tracing

Allen, C.W., *Astrophysical Quantities*. Athlone Press, 1976.

Ciddor, P.E. Refractive index of air: new equations for the visible and near infrared. *Applied Optics*, 35, 1566-1573, 1996.

Edlén, B., The Refractive Index of Air, *Metrologia*, 2, 71-80, 1966.

Birch, K. P., and M. J. Downs, An Updated Edlén Equation for the Refractive Index of Air, *Metrologia*, 30, 155-162, 1993.

Birch, K. P., and M. J. Downs, Correction to the Updated Edlén Equation for the Refractive Index of Air, *Metrologia*, 31, 315-316, 1994.

Coleman, C. D., W. R. Bozman, and W. F. Meggers, *Table of Wavenumbers*, US Department of Commerce, NBS Monograph 3, May, 1960.

A.3.1.5 Non-LTE

Funke, B. and M. Lopez-Puertas, Nonlocal thermodynamic equilibrium vibrational, rotational, and spin state distribution of NO($v=0,1,2$) under quiescent atmospheric conditions, *J. Geophys. Res.*, 105, 4409-4426, 2000.

A3.3.2.3: Global Land Cover Characteristics Data Base

Anderson, J.R., E.E. Hardy, J.T. Roach and R.E. Witmer, A land use and land cover classification system for use with remote sensor data, *U.S. Geological Survey Professional Paper* 964, 28, 1976.

Belward, A.S., ed., The IGBP-DIS global 1 km land cover data set (DISCover)-proposal and implementation plans, *IGBP-DIS Working Paper No. 13*, Toulouse, France, 1996.

Brown, J.F., T.R. Loveland, J.W. Merchant, B.C. Reed, and D.O. Ohlen, Using multisource data in global land cover characterization: concepts, requirements and methods, *Photogrammetric Engineering and Remote Sensing*, 59, 977-987, 1993.

Brown, J.F., B.C Reed, and L. Huewe, Advanced strategy for multi-source analysis and visualization in land cover characterization, *Proceedings, Pecora 13, Human Interactions with the Environment: Perspectives From Space*, in press.

Loveland, T.R., J.W. Merchant, J.F. Brown, D.O., Ohlen, B.C. Reed, P. Olson, and J. Hutchinson, Seasonal land-cover regions of the United States, *Annals of the Association of American Geographers*, 85, 2, 339-355, 1995.

Loveland, T.R., J.W. Merchant, D.O. Ohlen, and J.F. Brown, Development of a land-cover characteristics database for the conterminous U.S., *Photogrammetric Engineering and Remote Sensing*, 57, 11, 1453-1463, 1991.

Loveland, T.R., D.O. Ohlen, J.F. Brown, B.C. Reed, Z. Zhu, J.W. Merchant, and L. Yang, Western hemisphere land cover-progress toward a global land cover characteristics database, *Proceedings, Pecora 13, Human Interventions with the Environment: Perspectives From Space*, in press.

Olson, J.S., 1994a, *Global ecosystem framework-definitions*, USGS EROS Data Center Internal Report, Sioux Falls, SD, 1994.

Olson, J.S., 1994b, *Global ecosystem framework-translation strategy*, USGS EROS Data Center Internal Report, Sioux Falls, SD, 1994.

Zhu, Z., and L. Yang, Characteristics of the 1-km AVHRR data set for North America, *International Journal of Remote Sensing*, 17, 1915-1924, 1996.

A3.3.8.1: ABSCO DATABASES: Line Parameters

Arlander, D. W., Barbe, A., Bourgeois, M. T., Hamdouni, A., Flaud, J.-M., Camy-Peyret, C. and Demoulin, Ph., The identification of $^{16}\text{O}^{18}\text{O}^{16}\text{O}$ and $^{16}\text{O}^{16}\text{O}^{18}\text{O}$ ozone isotopes in high resolution ground-based FTIR spectra, *Journal of Quantitative Spectroscopy & Radiative Transfer*, 52, 267-271, 1994.

Birk, M. and G. Wagner, A new spectroscopic database for chlorine nitrate, poster session 2, Sixth Biennial HITRAN Database Conference, Harvard-Smithsonian Center for Astrophysics, Cambridge, MA, 19-21 June 2000.

Brown, L. R.; Gunson, M. R.; Toth, R. A.; Irion, F. W.; Rinsland, C. P.; and Goldman, A.: The 1995 Atmospheric Trace Molecule Spectroscopy (ATMOS) Linelist. *Appl. Opt.*, 35, 2828-2848, 1996.

Chackerian, C. and R. Freedman, New Electric Dipole Moment Unction for CO and Update of HITRAN CO Line Intensities, poster presentation, Workshop on laboratory spectroscopic needs for atmospheric sensing, San Diego, CA, 2001.

Cleveau, C.; Camy-Peyret, C.; Valentin, A. and Flaud, J.-F.: Absolute intensities of the ν_1 and ν_3 bands of $^{16}\text{O}_3$, *J. Mol. Spectrosc.*, 206, 115-125, 2001.

Dana, V.; Mandin, J.-Y.; Allout, M.-Y.; Perrin, A.; Régalia, L.; Barbe, A.; Plateaux, J.-J.; and Thomas, X.: Broadening parameters of NO_2 Lines in the 3.4 μm Spectral Region, *J. Quant. Spectrosc. Radiat. Transfer*, 57, 445-457, 1997.

Daumont, L.; Vander Auwera, J.; Teffo, J.-L.; Perevalov, V. I.; and Tashkun, S. A.: Line intensity measurements in $^{14}\text{N}_2^{16}\text{O}$ and their treatment using the effective dipole moment approach. *J. Mol. Spectrosc.*, 208, 281-291, 2001.

- Flaud, J.-M.; Camy-Peyret, C.; A. Mahmoudi, and Guelachvili, G.: The ν_2 band of HD^{16}O , *Internat. J. Infrared and Millimeter Waves*, 7, 1063-1090, 1986.
- Flaud, J.-M.; Bougeois, M. T.; Barbe, A.; Plateaux, J. J.; and Camy-Peyret, C.: The $\nu_1 + \nu_3$ bands of $^{16}\text{O}^{18}\text{O}^{16}\text{O}$ and $^{16}\text{O}^{16}\text{O}^{18}\text{O}$, *J. Molec. Spectrosc.*, 165, 464-469, 1994.
- Goldman, A.; Schoenfield, W.G.; Stephen, T. M.; Murcray, F. J.; Rinsland, C.P.; Barbe, A.; Hamdouni, A.; Flaud, J.-M.; and Camy-Peyret, C.: Isotopic ozone in the 5 μm Region from High Resolution Balloon-Borne and Ground-Based FTIR Solar Spectra. *J. Quant. Spectrosc. Radiative Transfer* 59, 231-244, 1998.
- Goldman, A.; Coffey, M. T.; Stephen, T. M.; Rinsland, C. P.; Mankin, W. G. and Hannigan, J. W.: Isotopic OCS from high-resolution balloon-borne and ground-based infrared solar absorption spectra. *J. Quant. Spectrosc. Radiative Transfer*, 67, 447-455, 2000.
- Heyart, M.; Perrin, A.; Flaud, J.-M.; Camy-Peyret, C.; Rinsland, C. P.; Smith, M. A. H.; and Malathy Devi, V., The ν_1 and ν_3 bands of $^{16}\text{O}^{17}\text{O}^{16}\text{O}$ line positions and intensities, *J. Molec. Spectrosc.*, 156, 210-216, 1992.
- Heyart, M., Perrin, A., Flaud, J.-M., Camy-Peyret, C., Rinsland, C. P., Smith, M. A. H. and Malathy Devi, V., The hybrid-type bands ν_1 and ν_3 of $^{16}\text{O}^{16}\text{O}^{17}\text{O}$ line positions and intensities, *J. Molec. Spectrosc.*, 157, 524-531, 1993.
- Jacquinet-Husson, N., et al., The 1997 spectroscopic GEISA databank. *J. Quant. Spectrosc. Radiative Transfer*, 62, 205-254, 1999.
- Jacquinet-Husson, N.; Scott, N.; Chédin, A.; and Chursin, A.: The current Geisa spectroscopic database system and Its Evolution. 6th Biennial HITRAN database conference, Harvard-Smithsonian Center for Astrophysics, Cambridge, MA 2000.
- Maté, B.; Lugez, C. L.; Solodov, A. M.; Fraser, G. T.; and Lafferty, W. J.: Investigation of the Collision-induced absorption by O_2 near 6.4 μm in pure O_2 and O_2/N_2 mixtures. *J. Geophys. Res.* 105 22,225-22,230, 2000.
- Malathy Devi, V.; Benner, D. C.; Rinsland, C. P.; Smith, M. A. H.; and Parmar, D. S.: Infrared Spectroscopy of the CO_2 Molecule: *Research Signpost: Recent Research Developments in Geophysical Research*, Vol. 1, pp. 119-148, S. G. Pandalai, editor, 1997.
- Malathy Devi, V.; Benner, D. C.; Rinsland, C. P.; and Smith, M. A. H.: Absolute Rovibrational Intensities of $^{12}\text{C}^{16}\text{O}_2$ Absorption Bands in the 3090 to 3800- cm^{-1} Spectral Region. *J. Quant. Spectrosc. Radiat. Transfer*, 60, 741-770, 1998a.
- Malathy Devi, V.; Benner, D. C.; Smith, M. A. H.; and Rinsland, C. P.: Pressure-Broadening and Pressure Shift Coefficients in the $2\nu_2^0$ and ν_1 Bands of $^{16}\text{O}^{13}\text{C}^{18}\text{O}$. *J. Quant. Spectrosc. Radiat. Transfer*, 60, 771-783, 1998b.

Malathy Devi, V.; Benner, D. C.; Smith, M. A. H.; and Rinsland, C. P.: Air- and N₂ Broadening Coefficients and Pressure-shift Coefficients in the ¹²C¹⁶O₂ Laser Bands. *J. Quant. Spectrosc. Radiat. Transfer*, 59, 137-150, 1998c.

Malathy Devi, V., Benner, D.C. Smith, M.A.H., Rinsland, C.P., and Dulick, M., Pressure-broadening and Pressure-Shift Coefficients in the ¹²C¹⁶O₂ and ¹³C¹⁶O₂ Laser Bands, *J. Mol. Spectrosc.*, in preparation, 2002.

Moyer, M. J.; Irion, F. W.; Gunson, M. R.; Rinsland, C. P.; Yung, Y. L.; and Gunson, M. R.: ATMOS stratospheric deuterated water and implications for tropospheric stratospheric exchange, *J. Geophys. Res. Lett.*, 23, 2385-2388, 1996.

Miller, C., High-resolution spectroscopy of CO₂ in the 4500- to 8000-cm⁻¹ region, poster presentation, Workshop on laboratory spectroscopic needs for atmospheric sensing, San Diego, CA, 2001.

Perrin, A.; Flaud, J.-M.; Goldman, A.; Camy-Peyret, C.; Lafferty, W. J.; Arcas, Ph.; and Rinsland, C.P.: NO₂ and SO₂ Line Parameters: 1996 HITRAN update and New Results, *J. Quant. Spectrosc. Radiat. Transfer*, 60, 839-850, 1998.

Perrin, A.; Rinsland, C. P. and Goldman, A.: Spectral parameters for the ν₆ Region of HCOOH and its measurement in the infrared tropospheric spectrum, *J. Geophys. Res.*, 104, 18,661-18,666, 1999.

Perrin, A.; Orphal, J., Flaud, J.-M.; Himmelmann, S.; Voigt, S.; Burrows, J.P.; Stephen, T. M. Goldman, A.; and Rinsland, C. P.: Recent Progress Achieved in the 6.2 μm Region for Nitrogen Dioxide. 6th Biennial HITRAN database conference, poster P22, Harvard-Smithsonian Center for Astrophysics, Cambridge, MA 2000.

Perrin, A., Flaud, J.-M.; Keller, F.; Goldman, A.; Blatherwick, R. D.; Murcray, F. J.; and Rinsland, C. P.: New analysis of the ν₈ + ν₉ band of HNO₃: Line positions and intensities, *J. Molec. Spectrosc.*, 194, 113-123, , 1999.

Perrin, A., J.-M.; Flaud, J.-M.; Keller, F.; Smith, M. A. H.; Rinsland, C. P. Malathy Devi, V.; Benner, D. C.; Stephen, T. M.; and Goldman, A.; The ν₁+ν₃ bands of ¹⁶O¹⁷O¹⁶O and ¹⁶O¹⁶O¹⁷O isotopomers of ozone, *J. Mol. Spectrosc.*, 207, 54-59 , 2001.

Pine, A. S., and C. P. Rinsland, The role of torsional hot bands in modeling atmospheric ethane, 53rd International Symposium on Molecular Spectroscopy Symposium, Columbus, OH, paper TF17, 1998.

Orlando, J.; Tyndall, G. S.; Nickerson, K.; and Calvert, J. G.: The Temperature Dependence of Collision-Induced Absorption by Oxygen near 6 μm. *J. Geophys. Res.* 96, 20,775-20,760, 1991.

Rinsland, C. P.; Flaud, J.-M.; Goldman, A.; Perrin, A.; Camy-Peyret, C.; Smith, M. A. H.; Malathy Devi, V.; Benner, D. C.; Barbe, A.; Stephen, T. M.; and Murcray, F. J.: Spectroscopic Parameters for Ozone and Its Isotopes: Current Status, Prospects for Improvement, and the Identification of $^{16}\text{O}^{16}\text{O}^{17}\text{O}$ and $^{16}\text{O}^{17}\text{O}^{16}\text{O}$ Lines in Infrared Ground-Based and Stratospheric Solar Absorption Spectra. *J. Quant. Spectrosc. Radiat. Transfer*, **60**, 803-814, 1998a.

Rinsland, C. P.; Gunson, M. R.; Wang, P.-H.; Arduini, R. F.; Baum, B. A. Minnis, P.; Goldman, A.; Abrams, M. C.; Zander, R.; Mahieu, E.; Salawitch, R. J.; Michelsen, H. A.; Irion, F. W.; and Newchurch, M. J.: ATMOS-ATLAS-3 Infrared Profile Measurements of Trace Gases in the November 1994 Tropical and Subtropical Upper Troposphere, *J. Quant. Spectrosc. Radiat. Transfer*, **60**, 803-814, 1998b.

Rinsland, C. P.; Jones, N. B.; Connor, B. J.; Logan, J. A.; Pougatchev, N. S.; Goldman, A.; Murcray, F. J.; Stephen, T. M.; Pine, A. S.; Zander, R.; Mahieu, E.; and Demoulin, E.: Northern and Southern Hemisphere Ground-Based Infrared Spectroscopic Measurements of Tropospheric Carbon Monoxide and Ethane, *J. Geophys. Res.*, **103**, 28,197-28,218, 1998c.

Rothman, L. S.; Rinsland, C. P.; Goldman, A.; Massie, S. T.; Edwards, D. P.; Flaud, J.-M.; Perrin, A.; Camy-Peyret, C.; Dana, V.; Mandin, J.-Y.; Schroeder, J.; McCann, A.; Gamache, R. R.; Wattson, R. B.; Yoshino, K.; Chance, K. V.; Jucks, K. W.; Brown, L. R.; Nemtchinov, V.; and Varanasi, P.: *J. Quant. Spectrosc. Radiat. Transfer*, **60**, 665-710, 1998.

Sen, B.; Toon, G. C.; Osterman, G. B.; Blavier, J.-F.; Margitan, J. J.; Salawitch, R. J.; and Yue, G. K. Measurements of reactive nitrogen in the stratosphere, *J. Geophys. Res.*, **103**, 3571-3585, 1998.

Smith, M. A. H.; Harvey, G. A.; Pellett, G. L.; Goldman, A.; and Richardson, D. J.: Measurements of the HCN ν_3 band broadened by N_2 . *J. Mol. Spectrosc.*, **105**, 105-112, 1984.
Smith, M. A. H.; Malathy Devi, V.; Benner, D. C.; and Rinsland, C. P.: Absolute intensities of $^{16}\text{O}_3$ lines in the 9-11 μm region, *J. Geophys. Res.*, **106**, 9909-9921, 2001.

Toth, R. A.: Water vapor measurements between 590 and 2582 cm^{-1} : Line Positions and Strengths. *J. Mol. Spectrosc.*, **190**, 379-396, 1998.

Thibault, F.; Menoux, V.; Doucen, R.; Rosenmann, L.; Hartmann, J.-M.; and Boulet, C.: Infrared collision-induced absorption by O_2 near 6.4 μm for atmospheric applications: Measurements and empirical modeling. *Appl. Opt.* **36**, 563-567, 1997.

Toon, G. C., J.-F. Blavier, B. Sen, and B. J. Drouin, Atmospheric COCl_2 measured by solar occultation spectroscopy. *Geophys. Res. Lett.*, **28**, 2835-2838, 2001.

Wang, W. F., Ong, P. P.; Tan, T. L.; Looi, E. C.; and Teo, H. H., Infrared Analysis of the Anharmonic Resonance between $\nu_8 + \nu_9$ and the Dark State $\nu_6 + \nu_7$ of HNO_3 . *J. Mol. Spectrosc.* **183**, 407-412, 1997.

Worden, H., Beer, R.; Rinsland, C. P.: Airborne infrared spectroscopy of western wildfires, *J. Geophys. Res.*, 102, 1287-1299, 1997.

Xu, L.-H.; Lees, R. M., Benchmark Laboratory Methanol Data at the University of New Brunswick, Canada. Session 4, Spectroscopic Parameters, 6th Biennial HITRAN database conference, Harvard-Smithsonian Center for Astrophysics, Cambridge, MA 2000.

LAST PAGE